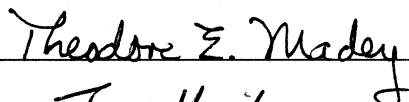



REVERSIBLE WETTABILITY OF NANOSCALE ZnO
ARRAYS

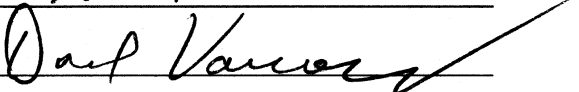
BY ANDREAS JOHANNES NUBER

A thesis submitted to the
Graduate School—New Brunswick
Rutgers, The State University of New Jersey
in partial fulfillment of the requirements
for the degree of
Master of Science
Graduate Program in Physics and Astronomy

Written under the direction of
Prof. Theodore Madey
and approved by







New Brunswick, New Jersey

October, 2005

ABSTRACT OF THE THESIS

Reversible wettability of nanoscale ZnO arrays

by **Andreas Johannes Nuber**

Thesis Director: Prof. Theodore Madey

This thesis describes an investigation of contact angles (CA) and their controlled changes on a zinc oxide “nanotips” surface grown by metalorganic chemical vapor deposition (MOCVD). The nanostructured surface consists of a dense array of slender ZnO nanotips with a high aspect ratio. The height of the tips used for this study is on the order of 500 nm, and the average width is about 80 nm. UV irradiation changes the wettability of these ZnO surfaces from hydrophobic to hydrophilic within 5 to 30 min, depending on the intensity of the radiation. By storing the sample in the dark for many hours, the hydrophilic surface reverts to hydrophobic. The reversible transition from hydrophilic to hydrophobic requires much more time than the process hydrophobic to hydrophilic caused by exposure to UV light. By keeping the sample in an oxygen atmosphere at 50°C we could shorten the recovery time for low to high contact angles from at least a month down to 20 hours. The measured contact angle minima and maxima, respectively, were $CA < 5^\circ$ and $CA > 100^\circ$, respectively. On flat ZnO films the measured CA were only in a range of 45° to 90° . This wettability transition is investigated by means of contact angle measurements, x-ray photoelectron spectroscopy (XPS) and Fourier transform infrared spectroscopy (FTIR). XPS measurements showed no correlation between concentration of oxygen-containing species and CA changes. Carbon

contamination in the vacuum systems, however changed the CA during the measurements to high values on the order of 100° . The estimated hydrocarbon layer thickness is less than 6 Å. FTIR studies indicate that adding and removing of hydrocarbons probably plays a role in the CA change since they are almost completely removed by UV irradiation and added again after recovery from low to high CAs. Hence even a hydrocarbon layer of about 1 ML thickness affects the macroscopic property of surface wettability.

Acknowledgements

My sincere gratitude goes to Professor Theodore Madey, this work would not have been possible without his guidance and support during my studies at Rutgers University. I thank Ted for giving me the opportunity to get the great experience of working in his group.

My special thanks go to Jennie Zhang for a great teamwork and helpfulness. It was very pleasant to work together with Jennie.

I would also like to thank Dr. Boris Yakshinskiy for introducing me into the XPS system and for his helpfulness whenever I needed something.

Many thanks to Dr. Sandrine Rivillon for her support in questions about FTIR and IR-data interpretation

I also want to thank Prof. Yicheng Lu and Prof. Yves Chabal for their cooperation and discussions.

Dedication

*To my parents
Anne and Karl Nuber*

Table of Contents

Abstract	ii
Acknowledgements	iv
Dedication	v
List of Tables	viii
List of Figures	ix
1. Introduction	1
2. Theory of wetting rough surfaces	3
3. Properties of zinc oxide	11
3.1. Crystal structure and surfaces	12
3.2. Electronic structure	16
3.3. Surface chemistry	19
4. Instrumentation and experimental techniques	22
4.1. Growth of ZnO nanotips	22
4.2. X-ray photoelectron spectroscopy (XPS)	25
4.2.1. Electron analyzer	26
4.2.2. X-ray sources	27
4.2.3. Physical basics of XPS	27
4.2.4. Peak positions, shifts and lineshapes	28
4.2.5. Quantitative analysis and surface sensitivity	30
4.3. Infrared Spectroscopy	32
4.3.1. Molecular vibrations	32

4.3.2.	Vibrations induced by infrared radiation	34
4.3.3.	Fourier Transform Infrared Spectroscopy (FTIR)	37
4.3.4.	Potential of FTIR	43
4.4.	Contact angle measurement	45
5.	Experimental results and discussion	48
5.1.	Control of contact angle changes	48
5.1.1.	Contact angle procedures	48
5.1.2.	Contact angle measurements	49
5.1.3.	Minimization of the transition time low \rightarrow high CA	52
5.1.4.	CA hysteresis	53
5.1.5.	Flat films and N-doping	54
5.2.	XPS measurements	55
5.2.1.	Systems used	56
5.2.2.	Measurements	58
5.2.3.	Quantitative measurements	62
5.2.4.	Carbon contamination	65
5.3.	FTIR measurements	67
5.3.1.	Measurements	67
5.3.2.	Results	68
5.4.	Conclusion	70
	References	72
	Vita	75

List of Tables

4.1. Crystal structure and lattice parameters of ZnO, GaN, and Al ₂ O ₃ . . .	23
4.2. Spin-orbit splitting parameters	28
5.1. Core level peak positions in a survey scan of ZnO nanotips	58

List of Figures

2.1. Schematic of a droplet on a homogeneous, flat surface to illustrate Young’s equation	4
2.2. Projection of the actual and projected (geometric) area of a rough surface	5
2.3. Droplet on a rough surface after Wenzel; plot of $\cos(\theta_w)$ versus $\cos(\theta)$	6
2.4. Droplet on a rough surface which forms a composite interface after Cassie; plot of $\cos(\theta_c)$ versus $\cos(\theta)$	6
2.5. Plot of the cosines of the contact angles after Wenzel and Cassie as functions of the cosine of Young’s contact angle	8
3.1. Wurtzite crystal structure of ZnO viewed from four perspectives	12
3.2. Models of the non-polar $(10\bar{1}0)$ and $(11\bar{2}0)$ ZnO surfaces	14
3.3. Models of polar (0001) -Zn and $(000\bar{1})$ -O ZnO surfaces	15
3.4. Photoemission energy distributions used to determine the general electronic structure of the polar (0001) -Zn and $(000\bar{1})$ -O and the non-polar $(11\bar{2}0)$ and $(10\bar{1}0)$ surfaces of ZnO	17
3.5. Difference between UPS spectra taken at surface- and bulk-sensitive photon energies for the $(10\bar{1}0)$, (0001) -Zn and $(000\bar{1})$ -O surfaces of ZnO	18
4.1. Schematic of the MOCVD growth chamber	22
4.2. SEM image of ZnO nanotips grown on a Si(111) substrate	24
4.3. SEM image of ZnO nanotips grown on Si(111) in the dimensions we used for our CA experiments	25
4.4. Scheme of a concentric hemispherical analyzer CHA	26
4.5. Illustration of the increasing surface sensitivity at grazing angles for XPS	31
4.6. Morse potential with indicated energy levels of the anharmonic oscillator	33
4.7. FTIR sample geometries	36

4.8. The schematic of a dispersive grating infrared spectrometer	37
4.9. The schematic of a Michelson interferometer	38
4.10. Interferogram of ZnO nanotips on Si	42
4.11. Single-beam spektrum of ZnO nanotips	42
4.12. View through the telescope of a contact angle goniometer	46
4.13. Setup for computer-aided CA measurements	46
5.1. Images of drops taken during CA measurement	49
5.2. CAs at corresponding sample treatment steps	50
5.3. Contact angle on a ZnO nanotip surface grown on Si as a function of UV irradiation time	51
5.4. Lamp spectra of different arc lamps	52
5.5. Measured transmittance spectrum of the used filter	53
5.6. Image of a drop with syringe taken during measurement of a receding CA	54
5.7. SEM images of a ZnO film and N-doped ZnO nanostructures	55
5.8. Scheme of the XPS system Kratos	56
5.9. Scheme of the modified XPS system from Φ	57
5.10. XPS survey spectra of ZnO nanotips	59
5.11. Detail scans of the O1s, C1s and Zn2p _{3/2} peak	61
5.12. Plot of the fitted components of the O1s peaks as functions of the CA, sample angle 45°	63
5.13. Effect of inverted surface sensitivity enhancement	64
5.14. O1s peak measured with the Kratos system under a sample angle of 90°	64
5.15. Plot of the fitted components of the O1s peaks as functions of the CA, sample angle 90°	65
5.16. FTIR sample spectra after annealing, both with the same reference spec- trum taken directly after growth	68
5.17. FTIR Sample spectra after the first annealing, after the first UV irradi- ation and after the second annealing	69

Chapter 1

Introduction

In Asia the Lotus flower (*Nelumbo Nucifera*) is revered as a holy plant. It represents eternity, purity and divinity and is widely used as a symbol of life, fertility, ever-renewing youth and to describe feminine beauty, especially the eyes. The reason for this is twofold: the beauty of the blossom, and the fact that even when the lotus flower emerges from muddy water, the leaves are untouched by any dirt or water. This self-cleaning, water-repelling effect of the lotus leaves was discovered and investigated by Barthlott et. al. from the Universität Bonn in Germany [1]. They found that the surface structure as well as the chemical composition of the surface affects the wettability and contaminability. The surface of the lotus leaf is rough on micrometer and on nanometer scales due to cells that are coated with water-repellent waxy crystals.

Wenzel [2] as well as Cassie and Baxter [3] studied the influence of surface roughness on the observed contact angle (CA) which is a measure for surface wettability and is defined as the angle between the solid-liquid and the liquid-vapor interface of a drop sitting on a surface. They created models to describe contact angles on rough surfaces which conclude that surface roughness amplifies both wetting properties (hydrophilicity, $CA < 90^\circ$) and non-wetting properties (hydrophobicity, $CA > 90^\circ$). Since the largest measured CA on flat surfaces is about 120° , surface roughening enables attaining much higher values of CA, even greater than 170° [4–6]. Surfaces with contact angles higher than 150° are called “superhydrophobic”, surfaces with contact angles close to 0° are called “superhydrophilic”.

This describes an investigation of contact angles and their controlled changes on a zinc oxide “nanotips” surface grown by metalorganic chemical vapor deposition (MOCVD). The nanostructured surface consists of a dense array of slender ZnO nanotips with a

high aspect ratio. UV irradiation changes the wettability of these ZnO surfaces from hydrophobic to hydrophilic. A reversible effect is obtained by storing the sample in the dark, which takes much more time than the hydrophilic to hydrophobic change induced by exposure to UV radiation. It is important to get an understanding of the mechanisms of this process. With this understanding we hope to be able to control of wettability changes and, for example, shorten the transition time from hydrophilic to hydrophobic or increase the maximum CA as well as decrease the minimum CA. Highly hydrophobic surfaces have many applications in daily life as well as in industry due to their water-repelling effect which could inhibit, for example, snow sticking, contamination and oxidation [6–8]. Also highly hydrophilic surfaces have applications like anti-fog coatings [7]. The possibility of controlling the CA properties by means of UV irradiation makes nanostructured ZnO surfaces also interesting for nano-fluidics applications.

Chapter 2

Theory of wetting rough surfaces

The main measure for wettability is the contact angle. In case of a droplet of liquid on a solid it is defined as the angle θ between the surface of the solid (solid-liquid interface) and the liquid (liquid-vapor interface) (see Figure 2.1). If $\theta < 90^\circ$ a surface is called hydrophilic, if $\theta > 90^\circ$ it is called hydrophobic. To understand how this contact angle forms, let us make an energy consideration. Every surface or interface, respectively, needs a certain amount of energy to be formed. This energy can be understood, for example, by thinking about cleavage of a solid material. The energy for breaking the bonds during the cleavage minus the relaxation energy of the surface atoms is related to the absolute surface energy of the two newly created surfaces. Therefore the energy needed to form one unit area of an interface or surface, respectively, is called surface energy σ [J/m^2] or surface tension γ [N/m], which is specific for each interface. σ and γ are equal only if there are no strains. A more general expression, which also considers surface strains is the surface stress tensor [9]:

$$\sigma_{ij} = \gamma\delta_{ij} + \left. \frac{\partial\gamma}{\partial\epsilon_{ij}} \right|_T \quad (2.1)$$

Here σ_{ij} is the component of the surface stress tensor, ϵ_{ij} is the component of the surface strain tensor, γ is the surface tension and T is the temperature. For the further discussion we assume that $\sigma = \gamma$ which is true for liquids and solids with small strains.

An equilibrium state is reached if the energy is minimized. Therefore if the interfacial energy of the solid-liquid interface σ_{sl} is smaller than the interfacial energy of the solid-vapor interface σ_{sv} a liquid droplet tends to spread out and wet the surface of the solid. The other way around, if $\sigma_{sl} > \sigma_{sv}$ the liquid droplet tends to remain compact, and to form less solid-liquid interface. This can be visualized by surface tension forces that

have a fixed value corresponding to the surface energy of the interface and act along the boundaries. The equilibrium state and minimum in surface free energy, respectively, are reached when all three forces caused by the surface tension along the interfaces are in equilibrium. This relation is expressed in *Young's equation*:

$$\cos(\theta) = \frac{\sigma_{sv} - \sigma_{sl}}{\sigma_{lv}} \quad (2.2)$$

Where θ is the contact angle, σ_{ii} is the surface tension or surface free energy respectively. The indices stand for the different interfaces: solid-vapor (sv), solid-liquid (sl) and liquid-vapor (lv).

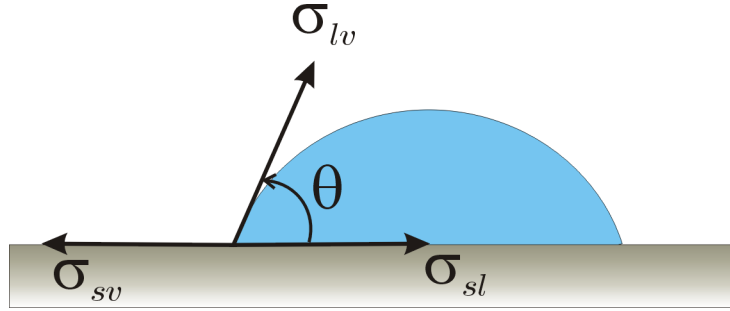


Figure 2.1: Schematic of a droplet on a homogeneous, flat surface. The arrows indicate the forces caused by the surface tensions σ_{ii} along the interfaces. The indices stand for the different interfaces solid-vapor (sv), solid-liquid (sl) and liquid-vapor (lv). θ is the contact angle between the surface of the solid and the liquid.

Young's equation is valid only for flat, smooth and chemical homogeneous surfaces. In reality this is usually not the case, therefore we have to look closer at rough surfaces. The theoretical basic principles of wetting rough surfaces were investigated by R.N. Wenzel, A.B.D. Cassie and S. Baxter. [2, 3]

Wenzel [2] made the assumption that the whole surface under the drop is covered with liquid. So with respect to a smooth surface there is more actual area wetted. We can define a roughness factor r as the ratio of the area of the actual and the projected, smooth surface.

$$r = \frac{\text{actual area}}{\text{projected area}} \quad (2.3)$$

Figure 2.2 shows a schematic cross section of the actual and projected or geometric

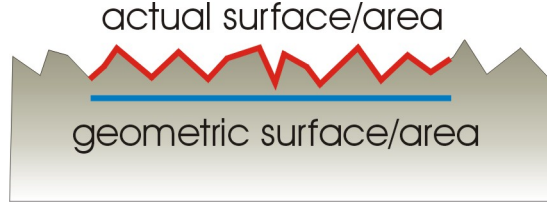


Figure 2.2: Projection of the actual and projected (geometric) area of a rough surface area, respectively, of a rough surface.

The contact angle is measured with respect to the projected surface plane. As the surface area of the solid with respect to a smooth surface is magnified by the roughness factor r , also the surface tension is magnified by r with respect to one unit area of the projected surface plane. The surface tension of the liquid is of course unaffected by the surface roughness of the solid. Therefore Young's equation has to be modified:

$$\sigma_{lv} \cdot \cos(\theta_w) = r \cdot (\sigma_{sv} - \sigma_{sl}) \quad (2.4)$$

$$\Rightarrow \cos(\theta_w) = r \cdot \frac{\sigma_{sv} - \sigma_{sl}}{\sigma_{lv}} \quad (2.5)$$

$$\Rightarrow \cos(\theta_w) = r \cdot \cos(\theta) \quad (2.6)$$

Where θ_w stands for the contact angle predicted by Wenzel's theory. Since r is always greater than one, surface roughness magnifies hydrophobic as well as hydrophilic properties of a surface. The relation between θ and θ_w is usually plotted as $\cos(\theta_w)$ as a function of $\cos(\theta)$. The graph is a linear function with slope r and cuts off at $\cos(\theta) = \pm 1/r$ because $\cos(\theta_w)$ cannot exceed 1. Figure 2.3 shows a droplet on a rough surface with wetting behavior after Wenzel and the plot of $\cos(\theta_w)$ versus $\cos(\theta)$.

Cassie and Baxter [3] used another approach. They also regarded a rough or porous surface. Since in the hydrophobic case the surface energy of the dry surface is lower than that of the wetted surface, the liquid does not follow all the surface contours but touches only the tips of the surface structure and creates a composite interface (see Figure 2.4(a)).

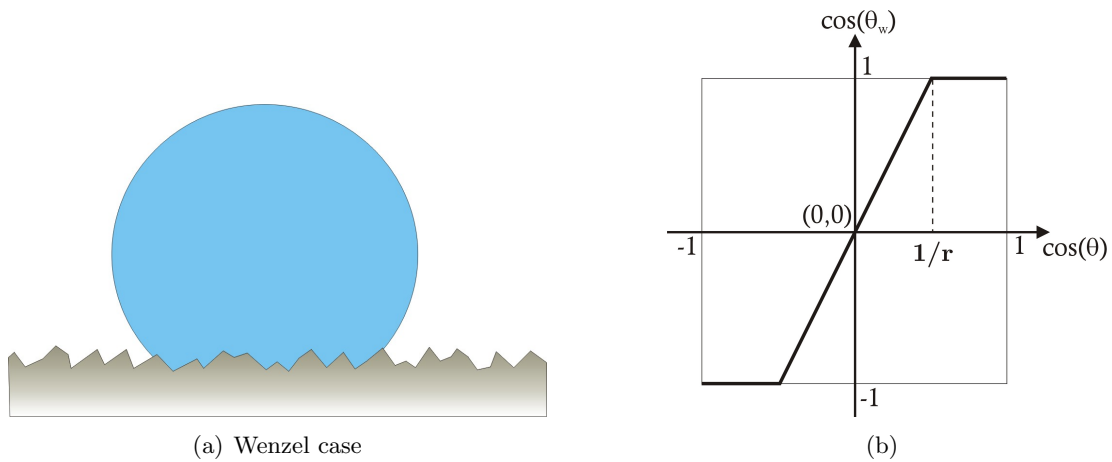


Figure 2.3: (a) Schematic of a droplet on a rough surface with wetting behavior after Wenzel. (b) in the Wenzel case $\cos(\theta_w)$ versus $\cos(\theta)$ is a linear function that cuts off at $\cos(\theta) = \pm 1/r$ because $\cos(\theta_w)$ can not exceed 1.

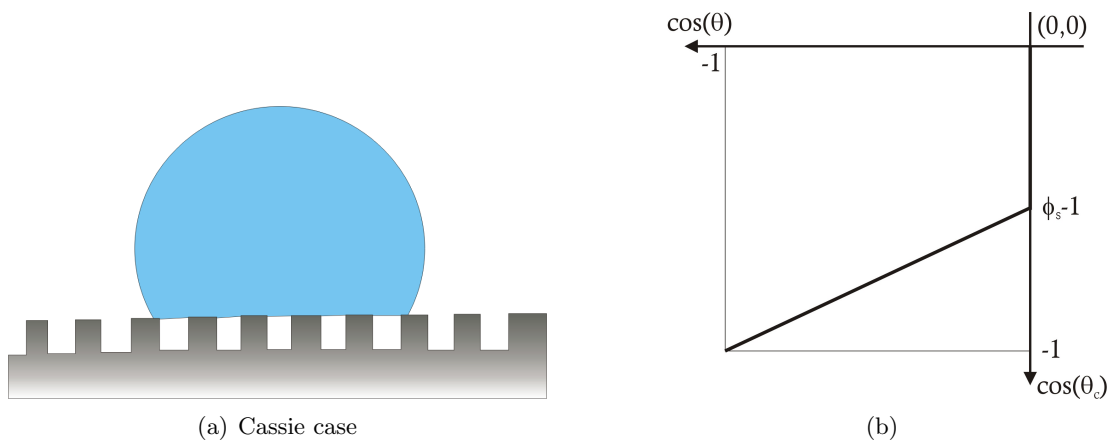


Figure 2.4: (a) Schematic of a droplet on a rough surface which forms a composite interface like Cassie proposed. (b) in the Cassie case $\cos(\theta_c)$ versus $\cos(\theta)$ is also a linear function but with a jump at $\cos(\theta) = 0$ to $\cos(\theta_c) = (\phi_s - 1)$.

The quantities σ_{lv} , σ_{sl} and σ_{sv} are defined as above, f_1 and f_2 are the total areas of solid-liquid interface and liquid-vapor interface respectively, created during formation of the composite interface. Therefore E_D is the expended energy for forming the composite interface:

$$E_D = f_1 (\sigma_{sl} - \sigma_{sv}) + f_2 \sigma_{lv} \quad (2.7)$$

Using Young's equation $\sigma_{lv} \cdot \cos(\theta) = (\sigma_{sv} - \sigma_{sl})$, E_D can be written as

$$E_D = \sigma_{lv} (f_2 - f_1 \cos(\theta)) \quad (2.8)$$

On a smooth surface, $(\sigma_{sl} - \sigma_{sv})$ is the energy E expended to form one unit area of solid-liquid interface. Thus

$$\cos(\theta) = \frac{-E}{\sigma_{lv}} \quad (2.9)$$

When E is positive, which indicates that increasing the solid-vapor interface increases the total surface energy, the minus sign in equation 2.9 results in a contact angle greater than 90° . By analogy, the following expression is valid for a composite interface:

$$\cos(\theta_c) = \frac{-E_D}{\sigma_{lv}} = f'_1 \cdot \cos(\theta) - f'_2 \quad (2.10)$$

Here θ_c is the contact angle predicted by Cassie and Baxter. E_D is now the energy expended to form one unit area of the composite interface, therefore f'_1 can be regarded now as the solid-liquid-fraction and f'_2 as the solid-vapor-fraction of the composite interface. Since there are only two components, we can write f'_1 as ϕ_s and f'_2 as $(1 - \phi_s)$ which gives the expression

$$\cos(\theta_c) = \phi_s \cdot \cos(\theta) + \phi_s - 1 \quad (2.11)$$

Figure 2.4(b) shows the plot of $\cos(\theta_c)$ versus $\cos(\theta)$. This graph is a linear function with slope ϕ_s and a jump at $\cos(\theta) = 0$ to $\cos(\theta_c) = (\phi_s - 1)$. This case makes physically

more sense for $\cos(\theta_c) \rightarrow -1$ since here, in contrast to the Wenzel model, $\cos(\theta_c) = -1$ is reached only asymptotically. Cassie's model is applicable only for hydrophobic surfaces since on a hydrophilic surface the water just follows the surface contours and fills the valleys which gives the condition for Wenzel's model.

Thus, in the case of a hydrophobic surface, there are two models to explain the observed contact angle. Both the Wenzel and Cassie models can be verified experimentally [4, 6]. So which is the right one to apply? An energy consideration shows that both states are local minima in surface free energy. Which state is reached depends on how the drop was formed. Pantakar [5] showed that the smaller contact angle of the two models is the global minimum. One state can be transformed into the other one; for example, a droplet in the Cassie state, sitting only on the tips of the rough surface structure, can be transformed into a droplet in the Wenzel state by pushing it down so that it wets all the surface beneath it. Both states are stable. For technical applications it is best to have a stable contact angle that does not change with influences from outside. The most stable contact angle is the one where both models have the same contact angle (see Figure 2.5). This can be achieved by controlling the

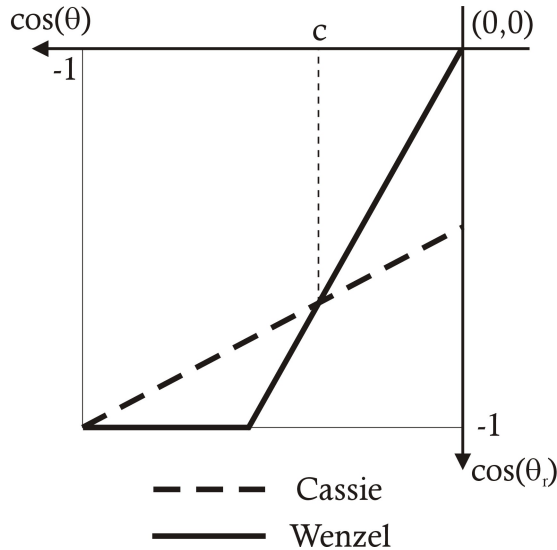


Figure 2.5: Cosine of the observed contact angle θ_r on a rough surface as a function of Young's contact angle θ in both models. At point c both contact angles are the same, so it is the most stable value.

surface geometry, for example by nanostructuring the surfaces. Bico et al. [4] created surfaces with defined surface structure and showed experimentally that modeling the surface structure allows to control the contact angle of a surface. They created surfaces with shallow cavities, stripes and spikes. All surface structures were periodic and in the micrometer range. The surface with spikes showed the highest contact angle of 170° . They verified both the Cassie/Baxter as well as the Wenzel equation. Since they put the droplet from above onto the surface, they usually got the Cassie state of the droplet forming a composite interface that wet only the tips of the structure. When they pressed on the droplet, the contact angle changed to the Wenzel state, wetting all the surface. The values of the contact angle agreed with the values predicted by Cassie's and Wenzel's equations, respectively.

On highly hydrophobic smooth surfaces, water has a contact angle on the order of 120° [10]. With surface roughening this contact angle can be increased to over 170° . Surfaces with such a high contact angle are called superhydrophobic. Per definition a surface is superhydrophobic if the contact angle $\theta > 150^\circ$. The counterpart is a superhydrophilic behavior with a contact angle close to 0° .

One problem in measuring contact angles is the fact that there is not one static contact angle on a surface but an advancing and a receding one. A way of measuring the hysteresis of contact angles is the method with a droplet on a tilted surface. Here the advancing contact angle is the one in direction of the drop movement where the solid-liquid-vapor contact line advances, the receding one, on the other side of the droplet, where the contact line recedes. Another way of measuring the advancing and the receding contact angle is by adding or withdrawing liquid from the drop. The advancing contact angle is the observed angle while the drop volume is increased, the receding one while the drop volume is decreased. All previous discussions and models predict the right values for the advancing contact angle but not for the receding one [4,5]. At the moment there is no significant model for receding contact angles. In order to get a water repellent self-cleaning surface, not the absolute value of the static contact angle is important but the dynamic wetting properties, namely the hysteresis of the contact angle is crucial [8]. Öner and McCarthy [8] explain this hysteresis with an energy barrier

for moving the solid-liquid-vapor contact line, which forms when the droplet comes to rest at a local energy minimum on a surface. Due to the no-slip boundary condition of fluid mechanics, which says that the velocity of a moving liquid in contact with a solid at the solid-liquid interface is 0, the only solid-liquid interfacial water molecules that have the possibility to move are the ones at the contact line. Therefore, the less stable the borderline, the less energy is necessary to move the droplet and the easier the droplet moves on the surface.

Chapter 3

Properties of zinc oxide

Zinc oxide occurs in nature as the mineral zincite or red zinc ore. Although natural crystals and locations where zincite can be found are rare around the world, Franklin, New Jersey is the most important and almost the only noteworthy site where natural zinc is found [11]. The red color of natural zincite is due mainly to its manganese content. Pure zinc oxide is white or transparent at room temperature but yellow at high temperatures. It occurs as hexagonal crystals or as white powder. The chemical composition of zinc oxide is ZnO. Its density is 5.68 g/cm^3 . Further it is amphoteric and soluble in both acids and bases but almost insoluble in water (0.005 g/l at 25°C). At ordinary pressure zinc oxide does not melt but sublimes at a temperature of $1975 \pm 25^\circ\text{C}$. ZnO is an *n*-type semiconductor with a wide direct bandgap of 3.3 eV at room temperature and a high exciton binding energy of 60 meV ; ZnO can show strong piezoelectric properties and luminescence. Furthermore it is transparent to visible light but opaque for UV light below 365.5 nm wavelength. [11]

The largest consumer of zinc oxide is the rubber industry. Here ZnO is used to shorten the time of vulcanization and for light colored rubbers as a reinforcement pigment. The second largest consumer is the paint industry. Zinc oxide powder, also known as zinc white, is used as a pigment in paints. Due to its opacity to UV light it improves the weatherability of coatings. Furthermore, it keeps its white color in contact with sulfur compounds in the atmosphere. Another large consumer of ZnO is the ceramics industry where it acts both as a network former and as a network modifier, e.g. in glass. Also, in the chemical industry zinc oxide is used, e.g. in the production of zinc soaps and other chemicals [11]. Due to its ability to absorb UV-light it is also a component of some ointments, creams, and lotions to protect against sunburn.

Further applications of zinc oxide are phosphors, surface acoustic wave devices, gas sensors, piezoelectric transducers, varistors, and transparent conducting films for the photovoltaic industry [12].

3.1 Crystal structure and surfaces

Zinc oxide crystallizes in the wurtzite structure which is the space group $P6_3mc$, No. 186 [13]. The lattice parameters are $a = 0.3249$ nm and $c = 0.5206$ nm [14]. It consists of two interpenetrating hexagonal closed packed (hcp) lattices of oxygen and zinc, respectively. The zinc cations are tetrahedrally coordinated with the oxygen ions and vice versa. The layers, which can be seen as built of Zn-O “dimers”, alternate in the stacking sequence ABABAB... . Figure 3.1 shows a schematic of the crystal structure of ZnO. There are four important low-index faces in the wurtzite structure.

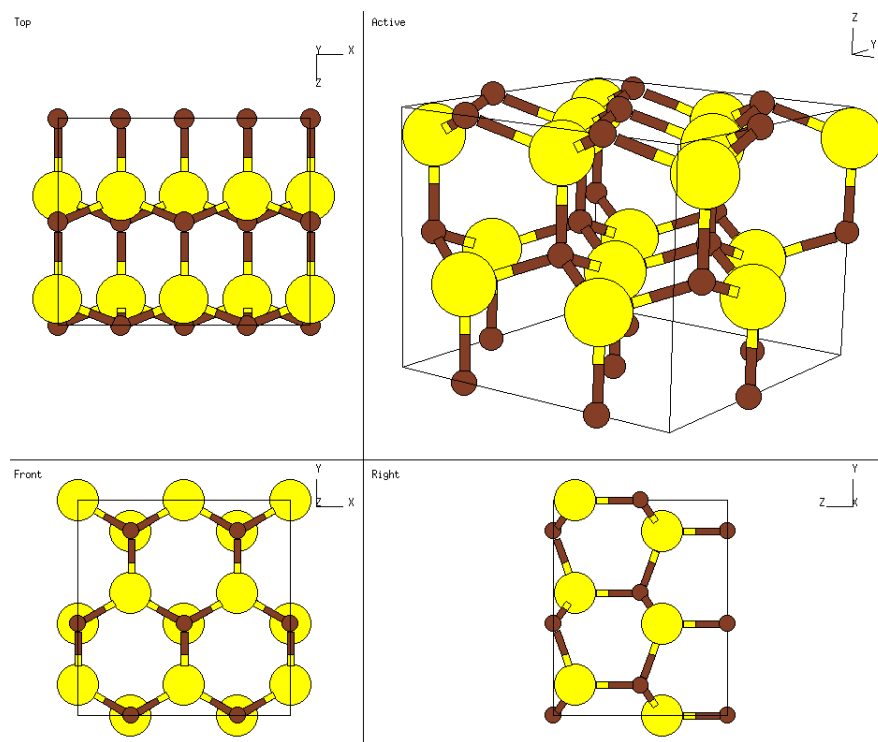


Figure 3.1: Wurtzite crystal structure of ZnO viewed from four perspectives. The small dark spheres represent the zinc ions, the larger spheres the oxygen ions. The z-direction in the schematic is the $[0001]$ direction in the hexagonal lattice and also called c-axis. (Figure taken from [15]).

The polar (0001) and (000 $\bar{1}$) surfaces, that are perpendicular to the c-axis, and the non-polar (10 $\bar{1}$ 0) and (11 $\bar{2}$ 0) surfaces which are parallel to the c-axis and are often called “prism” faces. The c-axis in a hexagonal lattice structure points towards the [0001] direction which is parallel to the z-axis in Figure 3.1. The dominant natural growth face is (000 $\bar{1}$). Figure 3.2 shows the two non-polar faces which have the same amount of cations and anions on the surface and are atomically flat. Each cation misses one of its tetrahedrally coordinated oxygen atoms with respect to the bulk lattice and each anion misses one zinc atom. For discussions concerning chemisorption it is sometimes useful to think of a “dangling bond” in the direction of the missing O-atom. On both faces the planes can be seen as being built by pairs or “dimers” of zinc and oxygen. Within the (10 $\bar{1}$ 0) surface the Zn-O pairs are aligned in rows and are bound to the atoms of the plane below rather than to each other (see Figure 3.2(a)). In the (11 $\bar{2}$ 0) plane the “dimers” are bound to the layer below as well as to each other which aligns them in zig-zag rows parallel to the c-axis (see Figure 3.2(b)). Qualitative LEED experiments [16] as well as STM experiments [17] show that the (10 $\bar{1}$ 0) is the most stable surface of ZnO and (11 $\bar{2}$ 0) is considerably less stable. After the surface cleaning procedures, LEED experiments on the (11 $\bar{2}$ 0) face showed spots originating from (01 $\bar{1}$ 0), (11 $\bar{2}$ $\bar{2}$) and (11 $\bar{2}$ $\bar{2}$) facets whereas the (10 $\bar{1}$ 0) surface showed no faceting. Other measurements were in qualitative agreement with the LEED results. [16] Quantitative measurements and theoretical calculations showed that the (11 $\bar{2}$ 0) surface is an ideal termination of the bulk structure within the accuracy of the measurements. The results for the (10 $\bar{1}$ 0) surface on the other hand showed that the zinc ions relax inward by 0.4 Å, whereas the oxygen ions stay on their bulk lattice locations. [16]

The wurtzite structure does not have a center of inversion. Hence, cleaving a zinc oxide crystal perpendicular to the c-axis, in the way that the fewest interatomic bonds were broken, leads to two different polar surfaces on the opposing faces. One of them is terminated by only zinc atoms and the other one by only oxygen atoms. Ideally, the (0001) surface is the one with only zinc atoms on the outermost layer and therefore also called (0001)-Zn face (see Figure 3.3(a)), the (000 $\bar{1}$) surface is terminated by oxygen and also called (000 $\bar{1}$)-O face (see Figure 3.3(b)). To maintain the charge neutrality each

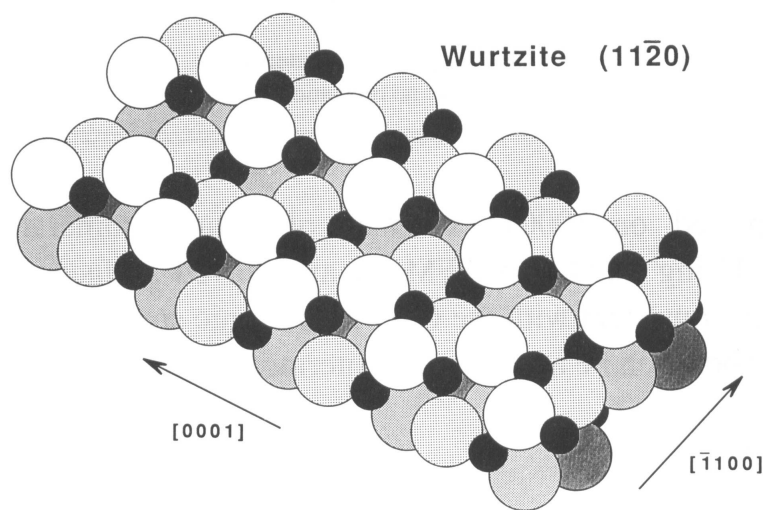
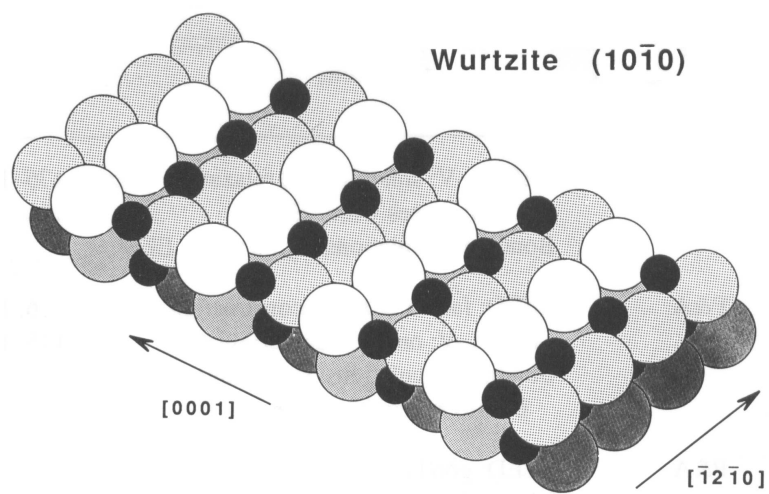


Figure 3.2: Models of the non-polar $(10\bar{1}0)$ and $(11\bar{2}0)$ ZnO surfaces, the smaller dark spheres represent zinc, the bigger bright ones oxygen: (a) $(10\bar{1}0)$ and (b) $(11\bar{2}0)$. (Figure taken from [16])

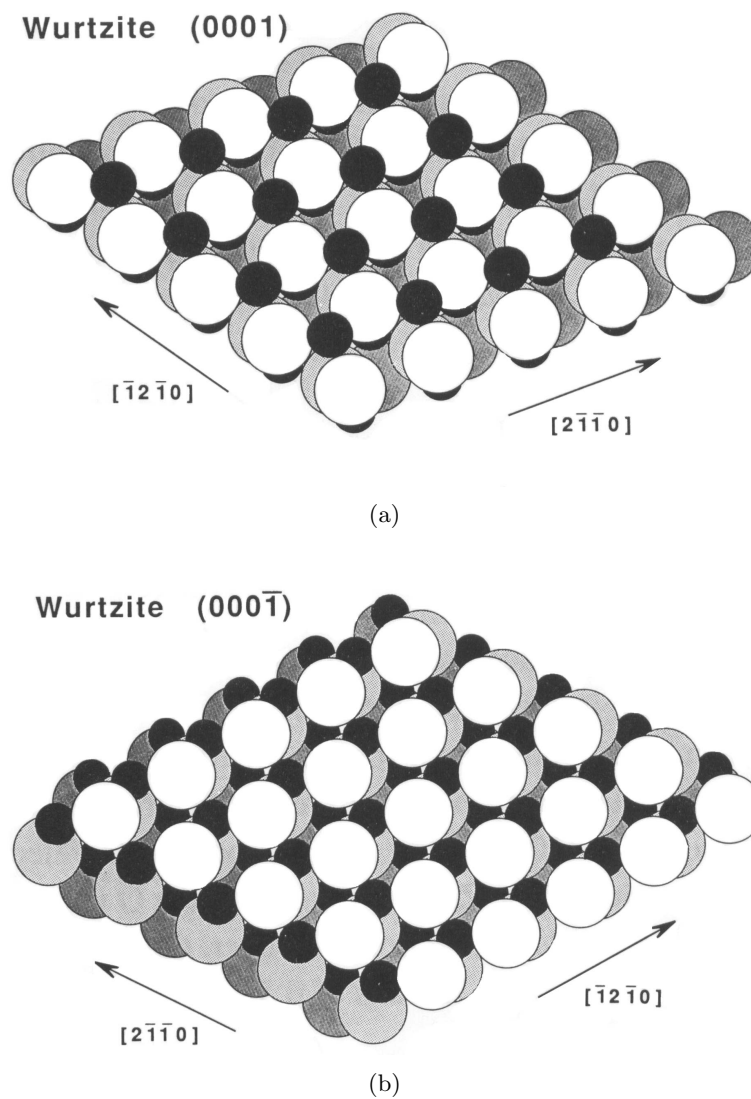


Figure 3.3: Models of polar (0001)-Zn and (000 $\bar{1}$)-O ZnO surfaces, the smaller dark spheres represent zinc, the bigger bright ones oxygen: (a) (0001) and (b) (000 $\bar{1}$). (Figure taken from [16])

crystal with an (0001) or (000 $\bar{1}$) surface must have the corresponding opposite face on the other side which is also observed experimentally. Due to the fact of having different atomic species on the outermost layer, the (0001) and (000 $\bar{1}$) surfaces act differently. For example the (0001)-Zn face barely reacts with HCl while the (000 $\bar{1}$) face is rapidly etched and becomes visibly roughened. [16] There is controversy concerning the stability of the two polar surfaces. There are qualitative LEED data on annealed surfaces that indicate that the (000 $\bar{1}$) surface is less stable because of additional beams originated from faceting and the poor quality LEED spots from the (000 $\bar{1}$) face. There are other LEED measurements that refer to similar quality and symmetry of the LEED spots of both surfaces. Recent STM studies show that the (0001)-Zn surface always shows a high density of small triangular holes and added islands, whereas the step heights are monatomic and terminated with O atoms which makes them non-stoichiometric and stabilizes this polar surface [17,18]. Also the (000 $\bar{1}$)-O surface has terraces but they are much smoother and the steps are of double height and stoichiometric [17]. The best fit to data for quantitative LEED I-V measurements of the (0001) face, interpreted in terms of dynamical multiple-scattering calculations, is with zinc ions relaxed inwardly by 0.2 Å. The measurements and simulations for the (000 $\bar{1}$) surface showed no relaxation of the oxygen ions, which can be explained by their size. [16] One proposed stabilization mechanism of the two polar surfaces is the charge transfer of 0.17 electrons from the (000 $\bar{1}$)-O surface to the (0001)-Zn surface which reduces the dipole moment [19].

3.2 Electronic structure

ZnO is a post-transition-metal oxide with a bandgap of 3.3 eV. It is usually a strong *n*-type semiconductor with electrons in the conduction band as charge carriers. The origin of this *n*-type conductivity is still controversial. Various donors have been proposed, e.g. oxygen vacancies, zinc interstitials or hydrogen doping [16,20,21]. Highly surface-sensitive angle-integrated UPS measurements on the four above-mentioned important low index surfaces show the general electronic structure of ZnO surfaces (Figure 3.4). The large peak at about 10 eV is produced by the filled Zn 3d band. The feature from 3 to 8 eV represents the valence band. According to theory the emission from 3 to 5 eV

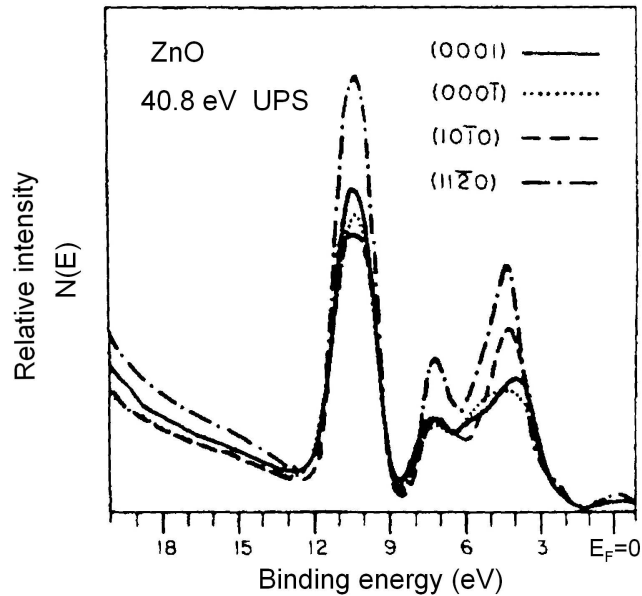


Figure 3.4: Photoemission energy distribution used to determine the general electronic structure of the polar (0001)-Zn and (000 $\bar{1}$)-O and the non-polar (11 $\bar{2}$ 0) and (10 $\bar{1}$ 0) surfaces of ZnO. Data measured with angle-integrated He II UPS. (Figure taken from [16]).

is from the non-bonding O 2p orbitals and the emission from 5 to 8 eV from a bonding combination of O 2p and Zn 4s orbitals. Although the Zn 3d band is very close to the valence band, the two are not considerably hybridized. The photoemission spectra are quite different between the four surfaces especially in the shape of the valence band. Figure 3.5 shows the difference between angle resolved UPS spectra taken at surface- and bulk sensitive photon energies, respectively. The surface sensitivity of photoelectron spectroscopy techniques depend on the escape depth of the measured electrons which is dependent on their kinetic energy. The kinetic energy of an escaping not-attenuated electron is basically the photon energy minus the binding energy and work function $E_{kin} = E_{h\nu} - E_{bind} - \phi$. In this particular case the photon energies were between 20 eV and 80 eV. Since the spectrum shows the valence band between 0 eV and 6 eV, the kinetic energies are comparable to the photon energies. In this energy range the electron escape depth for lower kinetic energies is greater than for higher ones. These difference spectra show the contributions of surface states and resonances. [16]

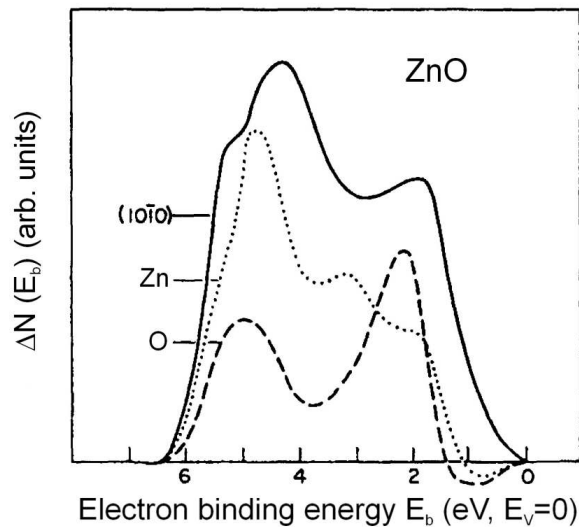


Figure 3.5: Difference between UPS spectra taken at surface- and bulk-sensitive photon energies for the $(10\bar{1}0)$, (0001) -Zn and $(000\bar{1})$ -O surfaces of ZnO, showing the contribution due to surface states and resonances. (Figure taken from [16]).

The work function ϕ of a metal oxide is extremely sensitive to the state of the surface. The slightest change in point defect densities, traces of adsorbed molecules, slight surface reconstruction, etc., can change the value of the work function significantly. Further, the work function is not uniform across a surface and different measuring techniques give different results. Therefore, the absolute value often is not of great importance. For example, published values of ϕ between 3.2 eV and 4.25 eV have been reported for the ZnO (0001) surface, depending on surface preparation and author [16]. Even for cleaved surfaces, different cleaves of the same crystal plane resulted in different values of ϕ and the values depended on the temperature at which the surface was cleaved. What can be seen is the trend

$$\phi(000\bar{1}) > \phi(10\bar{1}0) > \phi(0001)$$

and the work function of cleaved surfaces changes irreversibly upon annealing. [16]

The major surface defects on zinc oxide surfaces are oxygen vacancies. The removal of surface O^{2-} ions and, hence creating oxygen vacancies, does not create any new filled

electronic states in the bandgap, but results in an accumulation layer of the donated electronic charge. This accumulation layer is very sensitive to adsorbed molecules which results in changes of the surface conductivity. This makes ZnO a good material for gas sensors.

3.3 Surface chemistry

ZnO is an important material for both catalysis and gas sensor applications. Hence its chemisorption properties have been studied extensively. Gas sensor applications of ZnO are based on the change of surface conductivity which is very sensitive to adsorbed molecules. Charge transfer and band-bending caused by the adsorbates are the reason for this conductivity change. The corresponding surface chemistry of zinc oxide is very complex. Although a lot of experiments have been carried out on single crystal surfaces in order to get a basic understanding of the involved processes, the only general conclusion is that the chemisorption behavior of ZnO is very complicated. The diversity of polar and non-polar surfaces, the presence of acidic Zn and basic O sites, the complex and not yet well understood defect chemistry and the possibility of electron and oxygen transfer enable all sorts of chemisorption. These properties are the reason for the high catalytic and gas sensor activity of ZnO but also make it difficult to investigate the details of chemisorption mechanisms. There is a lot of contradiction between the results attained until now, and also between them and predictions of simple models. Hence there is still a lot of work to do in order to get a basic understanding. [16]

Hydrogen gas H_2 interacts very weakly with ZnO. It only physisorbs in molecular form onto stoichiometric ZnO surfaces below temperatures of 200 K. Its heat of adsorption, obtained from a Freundlich isotherm, is even lower than for Xe. Under low-pressure conditions there is practically no interaction detectable in surface science experiments, although it is known that H_2 dissociates on ZnO surfaces under catalytic high-pressure conditions, which is one of the steps in methanol synthesis from CO and H_2 . Atomic hydrogen H, on the other hand, interacts strongly with the ZnO (0001), (000 $\bar{1}$) and (10 $\bar{1}$ 0) surfaces. It acts as an electron donor and hence increases the surface conductivity of ZnO. Theoretically the adsorption of H onto the ZnO (000 $\bar{1}$) surface has

been studied via cluster calculations. With the assumption of H binding in on-top sites directly above surface O ions the calculation predicts strong O-H bonds where each H atom donates 0.5 electrons to the surface O ion. This charge transfer results in an increased surface conductivity and decreased work function due to the layer of positively charged H. Cluster calculations for adsorption of H atoms on the Zn (10 $\bar{1}$ 0) surface predicted both strong O-H and quite strong Zn-H bonds which results in neighboring Zn²⁺-H⁻ and O²⁻-H⁺ sites. [16]

O₂ interacts weakly with stoichiometric ZnO surfaces. Below room temperature it only physisorbs without any charge transfer between the surface and the molecule. Between 300 K and 650 K molecular oxygen chemisorbs and charge transfer from the surface to the O₂ occurs which changes the surface conductivity and results in adsorbed O₂⁻. Because of the small sticking coefficient of 10⁻⁵ at low coverages and measured coverages of less than 2.5 × 10⁻⁴ monolayers in the temperature range where chemisorption occurs, it is concluded that adsorption occurs on defect sites. This is also supported by experiments where O-vacancy point defects were created on a (10 $\bar{1}$ 0) surface by heating it to about 950 K and then quenching to room temperature, and afterwards absorbing O₂. The sticking coefficient increased exponentially with the defect density and the changes in surface conductivity were accordingly larger. Molecular oxygen most probably dissociates at defect sites generating atomic O that heals the surface defects to at least some extent, but also O₂⁻ adsorbs on defect surfaces. Oxygen adsorption was also studied on stepped surfaces like the (40 $\bar{4}$ 1) and the (50 $\bar{5}$ 1) surfaces. On the step edges the coordination of the cations is less than that on (10 $\bar{1}$ 0) terraces. At room temperature more oxygen adsorbs at these stepped surfaces. Thermal desorption experiments showed that most of the O₂ adsorbed in a more tightly bound state on the stepped surfaces than on the terraces. Even though more O₂ is adsorbed, the total oxygen coverage on stepped surfaces is still only a few % indicating that even at stepped surfaces the O₂-surface interaction is weak. [16]

Henrich and Cox state in “The Surface Science of Metal Oxides” [16] that water interacts very weakly with the (0001), (000 $\bar{1}$) and (10 $\bar{1}$ 0) ZnO surfaces; there is no evidence of dissociation into OH⁻ ions. Water (D₂O) chemisorbed at a temperature of

100 K was studied by means of thermal programmed desorption. The spectra showed six different desorption peaks for the three crystal faces. Three-dimensional ice was related to the peak at 152 K, two-dimensional ice to 168 K. Adsorption of the D_2O molecules at surface O sites was associated with a peak at 190 K because it did not appear on the Zn-terminated (0001) surface and since it was virtually not present on the O-terminated (000 $\bar{1}$) surface, the peak at 340 K was attributed to adsorption at surface Zn sites. The other peaks were thought to correspond to D_2O clusters or potentially to adsorption at interstitial Zn ions. A recent extensive study [22] of water adsorption on (10 $\bar{1}$ 0) ZnO surfaces concluded that water partially dissociates and forms a (2×1) superstructure with long-range order in which every second H_2O molecule is dissociated. This structure is stable from 200 K up to the boiling point of liquid water. He atom angular distributions and LEED showed both sharp half order diffraction peaks which indicates the (2×1) periodicity. STM measurements also showed this periodicity. Further, quantitative XPS measurements at full coverage revealed that there is one H_2O molecule per Zn ion adsorbed on the surface. The high binding energy of 1.02 eV was measured via the reflectivity of thermal energy He atoms as a function of surface temperature (He-TDS). Since such high desorption temperatures or binding energies, respectively, were observed only on few other metal oxide surfaces on which water is known to adsorb dissociatively, a dissociation of H_2O with hydroxylation of a surface O atom and adding a OH species on top of a surface Zn atom seems very probable. Together with theoretical calculations, which show it to be the most stable one, the following structure of adsorbed water is found. The H_2O molecules adsorb with their O atom on the surface Zn atoms which thus gain their four-fold tetrahedral bulk coordination. Every second molecule dissociates and the hydrogen atom is transferred to a substrate O atom. This structure is also stabilized by hydrogen bonds. One H atom forms a hydrogen bond to a neighboring substrate O atom, the other H atom forms a hydrogen bond to an adjacent dissociated adwater. The results of this study are quite unusual and most authors do not believe that molecular water adsorbs at temperatures over 300K.

Chapter 4

Instrumentation and experimental techniques

4.1 Growth of ZnO nanotips

The ZnO films and nanotips investigated in this thesis were grown by metalorganic chemical vapor deposition (MOCVD). Figure 4.1 shows a schematic of the vertical flow MOCVD reactor used. The functional principle of MOCVD is the reaction of precursors

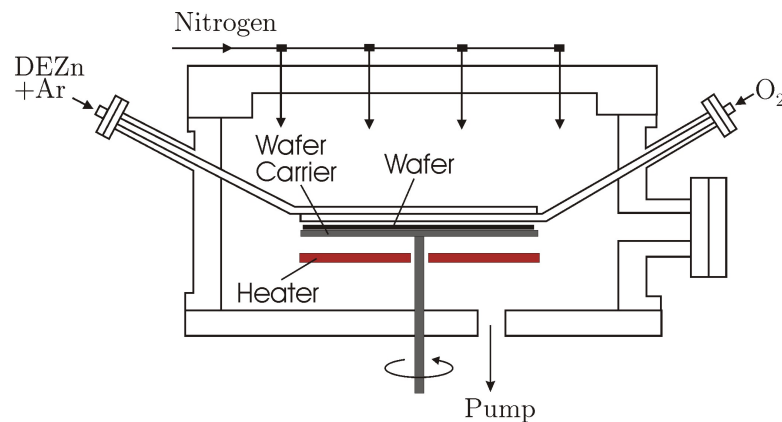


Figure 4.1: Schematic of the MOCVD growth chamber (Figure taken from [13]).

on a heated substrate. With the aid of carrier gases, the precursors are piped over the substrate. Due to the high temperature of the substrate and the oversaturation of the precursors in the gas-phase there occurs crystal growth on the substrate.

For the growth of the investigated ZnO films, diethyl zinc ($\text{DEZn}-(\text{CH}_3\text{CH}_2)_2\text{Zn}$) as metalorganic source and O_2 as oxidizer were used as precursors, N_2 and Ar were the carrier gases. Ultrahigh purity Ar is passed through a DEZn bubbler which is held at a temperature between 0°C and 20°C ; the vapor pressure of DEZn is in the range of 3.6 to 12.2 torr [13]. Oxygen and DEZn react strongly even at room temperature.

Hence they have to be introduced into the chamber separately to avoid pre-reaction in the gas-phase. The introduction of the precursors into the chamber occurs through injectors which extend horizontally near the surface of the substrate and have fine holes in them. ($\text{N}_2 + \text{Ar}$) flows continuously from the top of the chamber. The substrate is mounted on a susceptor (a plate on which a wafer may be heated during deposition steps) which can rotate with high speeds. The heating is achieved by radiation from a resistive heater placed below the wafer carrier. At optimized flow rates, rotation speeds and substrate temperatures a uniform growth can be obtained. Usual growth conditions are chamber pressures of 20 - 50 torr, a growth temperature of $300^\circ\text{C} - 500^\circ\text{C}$, rotation speeds of about 20 rpm, a total carrier gas flow from the top of 5000 - 15000 sccm, an O_2 flow of 1000 - 3000 sccm and an Ar flow through the DEZn bubbler of 100 sccm with an additional Ar flow of 1000 sccm introduced after the bubbler [13, 14]. 'sccm' is a common unit of gas flow in semiconductor processing and stands for standard cubic centimeters per minute which is a flow of 1 cm^3 of gas per minute at 0°C and at atmospheric pressure.

Zinc oxide grown on certain substrates like $c\text{-}/a\text{-Al}_2\text{O}_3$, GaN, fused silica, $\text{SiO}_2\text{-Si}$ and Si result in a columnar growth perpendicular to the substrate surface. The columns nucleate independently and an array of nanoscale fibers grows. On various orientations of Al_2O_3 and GaN, ZnO grows in dense smooth films but in some directions and certain growth conditions columnar growth occurs. Table 4.1 shows the crystal structure and lattice parameters of ZnO, GaN, and Al_2O_3 . ZnO grown on fused silica,

Crystal	Structure	Space Group	Lattice Parameter (\AA)
ZnO	Wurtzite (hexagonal)	$P6_3mc$	$a = 3.249$ $c = 5.206$
GaN	Wurtzite (hexagonal)	$P6_3mc$	$a = 3.186$ $c = 5.178$
Al_2O_3	Corundum (rhombohedral, hexagonal packing of oxygen ions)	$R\bar{3}c$	$a = 4.758$ $c = 12.992$

Table 4.1: Crystal structure and lattice parameters of ZnO, GaN, and Al_2O_3 (Table taken from [23]).

on amorphous SiO_2 thermally grown on Si, and on Si with native oxide forms the

columnar structure. The epitaxial relationship between c-sapphire and ZnO is $(0001) \text{ ZnO} \parallel (0001) \text{ Al}_2\text{O}_3$ and $[10\bar{1}0] \text{ ZnO} \parallel [2\bar{1}\bar{1}1] \text{ Al}_2\text{O}_3$, whereas the epitaxial relationship between a-sapphire and ZnO is $(0001) \text{ ZnO} \parallel (11\bar{2}0) \text{ Al}_2\text{O}_3$ and $[11\bar{2}0] \text{ ZnO} \parallel [0001] \text{ Al}_2\text{O}_3$ [14]. Thus ZnO grows with the c-axis perpendicular to the substrate surface. In all films grown with columnar structure, the ZnO nanotips are preferably oriented along the c-axis. The nanorods are single crystals, have a high aspect ratio and are terminated in sharp nanoscale tips. Since ZnO is a polar semiconductor with (0001) planes being Zn-terminated and $(000\bar{1})$ planes being O-terminated, the two planes have different polarity and therefore a different surface energy. This results in a high growth rate in direction of the c-axis and therefore in columnar growth. The columns usually are Zn-terminated [14, 23].

Figure 4.2 shows SEM images of ZnO nanotips grown on a Si(111) substrate. The

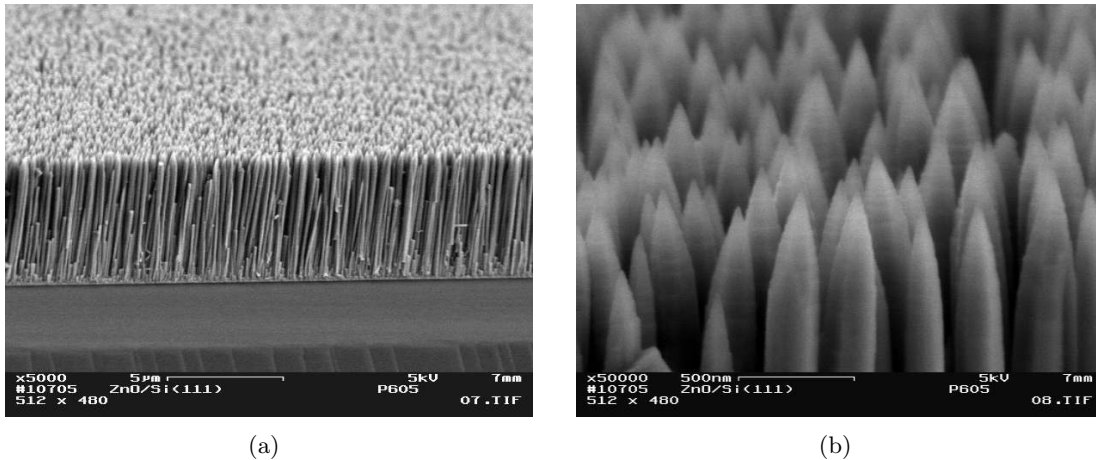


Figure 4.2: (a) SEM image of ZnO nanotips grown on a Si(111) substrate, the dense needle like structure is clearly visible; (b) magnified SEM image of the vertices of ZnO nanotips grown on a Si(111) substrate.

dimensions of the tips vary with growth time and conditions. The longer the growth, the higher the tips and the greater the diameter. In Figure 4.2 the tips are about $5\mu\text{m}$ tall and about 200nm to 300 nm in diameter. These were grown relatively long (growth time 4h). Due to growth-time reasons, the typical dimensions of the nanotips we used for our CA experiments were a height of about 500nm, a diameter of about 80nm to 100nm and a sharp tip of about 5nm in size (growth time 30min). Figure 4.3 shows

a SEM image of a regular growth ZnO on Si(111) of the type we used for our CA experiments.

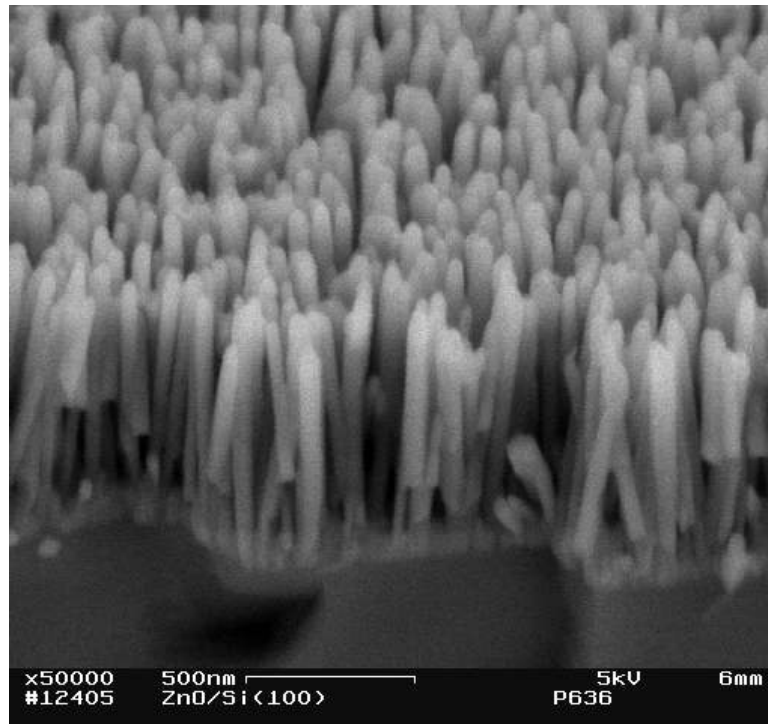


Figure 4.3: SEM image of ZnO nanotips grown on Si(111) with dimensions we used for our CA experiments.

4.2 X-ray photoelectron spectroscopy (XPS)

XPS is a powerful technique in surface analysis. It can detect and identify atomic species within the first few atomic layers of a surface and provide information about the surface composition, the chemical states of the elements involved and to a certain amount of the structure and thickness of layers on surfaces [24, 25]. Because of its capability of indicating the chemical state of atoms in compounds, XPS is also called ESCA - Electron Spectroscopy for Chemical Analysis. Within the following subsections the general basics of XPS are described. The actual settings and modes I used in my experiments are characterized later within the description of my actual experiments.

4.2.1 Electron analyzer

Since XPS is an electron spectroscopy, the kinetic energy of the photoelectrons emitted from the sample have to be measured. But before the electrons can enter the electron analyzer they have to travel a certain distance. In order that the electrons are not scattered by gas molecules and hence are lost for detection, the experiment has to be conducted under vacuum conditions. For typical spectrometer dimensions a pressure of about 10^{-6} torr is sufficient for that purpose. The reason why typically lower pressures are needed is the high surface sensitivity of XPS. Hence it has to be ensured that for the duration of the experiment only very few molecules will adsorb. For most experiments a base pressure of 10^{-10} torr should be adequate [25].

The most common electron analyzer for XPS is the concentric hemispherical analyzer CHA. It is an electrostatic deflection analyzer hence the electrons are deflected and focused on a detector by an electrostatic field. The CHA consists of two concentric metal hemispheres with radii R_1 (inner) and R_2 (outer) which are at different potentials $-V_1$ and $-V_2$ with $V_1 < V_2$ (see Figure 4.4). Since the relative resolution $R = \frac{\Delta E}{E}$ is

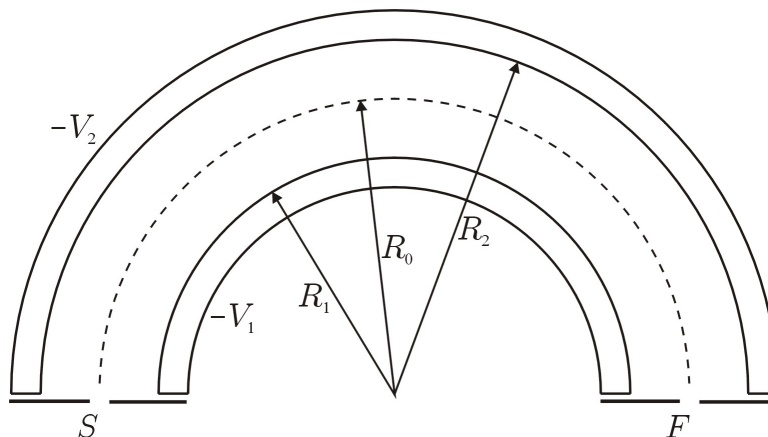


Figure 4.4: Scheme of a concentric hemispherical analyzer CHA with the inner radius R_1 and outer radius R_2 . The two hemispheres are at the potentials $-V_1$ and $-V_2$. S and F mark the entrance and exit slits, respectively. R_0 is the medial radius between R_1 and R_2 .

fixed by the analyzer geometry, the resolving power $\rho = \frac{E}{\Delta E}$ can be increased by retarding the electrons before entering the analyzer. With retardation of the electrons the

CHA can be operated in two modes, fixed retarding ratio (FRR) where the retarding ratio of the electrons is kept constant and fixed analyzer transmission (FAT) where the pass energy of the electrons is kept constant. An electron lens system can be used to focus the electrons on the entrance slit S and allows a more convenient working distance to the sample of at least 50mm [25]. CHA have a small acceptance angle of about 5° but a good energy resolution [24].

4.2.2 X-ray sources

In usual lab instruments, the x-rays are produced by bombarding a target with high energetic electrons which cause electron core holes. Hence the produced radiation is characterized by line emissions associated with filling the created core holes and a continuous background produced by Bremsstrahlung. The energy of the bombarding electrons is significantly higher than the K-shell binding energy of the target material. The emission spectrum is dominated by an unresolved doublet, $K_{\alpha_{1,2}}$ which is associated with decays from $2p_{\frac{1}{2}} \rightarrow 1s$ and $2p_{\frac{3}{2}} \rightarrow 1s$. But also other lines are present like $K_{\alpha_{3,4}}$ and K_{β} . The $K_{\alpha_{3,4}}$ in unmonochromatised sources can cause additional features in the XPS spectrum with about 8% of the main intensities at about 10 eV higher binding energies [24]. These additional features are called “ghost peaks”, but also features originating from any radiation other than the desired line are called “ghost peaks”. Other radiation sources could be impurities in the target material or emission from the Al or Be window that shields the sample and vacuum chamber from electrons from the x-ray source. Common target materials are aluminum (Al $K_{\alpha_{1,2}} = 1486.6$ eV, FWHM = 0.85 eV) and magnesium (Mg $K_{\alpha_{1,2}} = 1253.6$ eV, FWHM = 0.7 eV) [25].

4.2.3 Physical basics of XPS

In principle photoelectron spectroscopy is a simple process in which a photon of energy $h\nu$ penetrates the surface and is absorbed by an electron with binding energy E_b which hereon leaves the surface with the kinetic energy $E_{kin} = h\nu - E_b$ (Einstein relation). The kinetic energies of these photoelectrons leaving the surface can be measured and plotted as a spectrum. In the simplest case, this spectrum should simply be the energy

distribution of the electron states in the solid. In reality this process is, of course more complicated than this simple picture and a lot of factors have to be considered. These factors can, for example, shift the energetic position of the peaks, change their shape or even create additional features. Most of these modifications of the simple picture are caused by physical properties of, and processes in the sample but also the photon source and the properties of the spectrometer itself have to be considered.

The initial states in the sample from which the photoelectrons are excited are characterized by the angular momentum l ($l = 0, 1, 2, 3, \dots$) and the spin s ($s = \pm\frac{1}{2}$) of the electrons. In heavier atoms they couple together to the total angular momenta j of each electron which then couple to the total angular momentum of the whole atom J . This coupling is called “ j - j coupling” and is the reason why peaks from non- s -levels ($l > 0$) are doublets. The energy difference between these two levels ΔE_j is proportional to the spin-orbit coupling constant and reflects the “parallel” and the “anti-parallel” nature of the spin and angular momentum vectors of the according electron. ΔE_j increases with the atomic number Z for a given (l, n) and increases as l decreases for constant n . The ratio of the degeneracies $(2j + 1)$ gives the relative intensities of the according doublet peaks (see Table 4.2).

Subshell	j values	Area ratio
s	$\frac{1}{2}$	—
p	$\frac{1}{2}, \frac{3}{2}$	1 : 2
d	$\frac{3}{2}, \frac{5}{2}$	2 : 3
f	$\frac{5}{2}, \frac{7}{2}$	3 : 4

Table 4.2: Spin-orbit splitting parameters. (taken from [25])

4.2.4 Peak positions, shifts and lineshapes

The peak width ΔE is defined as full width at half maximum FWHM and is a convolution of several contributions. If all contributions have a Gaussian line shape, $\Delta E = (\Gamma^2 + \Delta E_p^2 + \Delta E_a^2)^{\frac{1}{2}}$, where Γ is the natural or inherent line width of the core level, ΔE_p is the line width of the x-ray source and ΔE_a is the analyzer resolution. Γ

reflects the uncertainty in the lifetime of the ion state after the photoemission. With the uncertainty principle we get $\Gamma = h/\tau$ eV, where h is Planck's constant and τ is the lifetime in seconds. Core hole lifetimes are determined by the processes after the photoemission in which the excited state relaxes or decays. There are three main processes involved. Either emission of an x-ray photon or emission of an electron in an Auger or in a Coster-Kronig process [25].

The kinetic energy with which the photoelectrons are emitted is $E_{kin} = h\nu - E_b - \phi$ where E_b is the binding energy with respect to the Fermi level and ϕ the work function is a "catch all" term which depends on the sample and the spectrometer. In practice the vacuum level is not the reference used for measuring the binding energy since it is hard to determine. The used reference is the Fermi-level of the sample which can be relatively easily determined in the spectrum since it is referred to the highest energy photoelectrons. With the emission of the photoelectron, another electron of the remaining atom can be excited into a higher bound state or being emitted into the continuum. This energy for the other electron has to be subtracted from the kinetic energy of the photoelectron and gives rise to features at higher binding energies. The discrete peaks caused by the excitation to a bound state are called "shake up", the continuous features caused by the excitation to the continuum are called "shake off". Solids can be excited in additional ways, for example, electron-hole pairs around the fermi level can be excited by the photoelectrons which results in an asymmetric lineshape for XPS photoelectron peaks. Also plasmons can be created which produces equidistant features at higher binding energies separated by integral multiples of the plasmon energy [24].

Another shift of the kinetic energy is called "chemical shift". Its name indicates that it is caused by the chemical environment of the emitting atom and hence of considerable practical value. It consists of two effects. The first effect is the influence of the chemical environment on the relaxation of the electrons during or after the emission of the photoelectron. The second effect, often called "true chemical shift", results from the shifted initial binding energy of the electrons due to the changed electronic environment. The chemical shift can be used to determine the chemical state of the detected atomic species. Quantitative analysis of the detected elements together with

the data about the chemical state can provide information about the stoichiometry of the measured compounds.

4.2.5 Quantitative analysis and surface sensitivity

For quantitative analysis the intensity and therefore the peak area contains the crucial information. The total intensity of a photoelectron signal N_i of a species i is composed of several components dN_i originating from positions, x, y, z and can be written as [24]:

$$\begin{aligned}
 dN_i = & (\text{x-ray flux at } x, y, z) \times (\text{no. of atoms of } i \text{ at } x, y, z) & (4.1) \\
 & \times (\text{different cross-section of relevant level of species } i) \\
 & \times (\text{probability of electrons escaping without energy loss from } x, y, z) \\
 & \times (\text{acceptance solid angle of electron analyzer}) \\
 & \times (\text{instrumental detection efficiency})
 \end{aligned}$$

The last two points are of instrumental nature, the x-rays penetration depth is much greater than the electron escape depth and can therefore mostly be regarded as uniform. Hence in order to get information about the atomic concentration of a species, mainly the cross-section of the relevant levels and the probability of the non-loss escape of the electrons have to be considered. In case of a homogeneous sample only the ionization cross-section has to be taken into account which is usually done by dividing the peak area by so-called “relative sensitivity factors” (RSF). These sensitivity factors are generally obtained by measurements of well known reference materials and can be transferred to XPS systems of the same type. Hence the values of RSFs are tabulated for various kinds of systems and do not necessarily have to be determined for every single system [25].

The surface sensitivity of XPS of typically only a few atomic layers is due to the small electron escape depth in solids. The electron attenuation in an overlayer of thickness d is given by $\exp(-d/\lambda)$, where λ is the electron attenuation length. Thus 95% of the intensity arises from a depth not deeper than 3λ if the electrons are measured at a take-off angle of 90° . The surface sensitivity can be enhanced by changing the take-off

angle to smaller values since the vertical depth sampled (for 95% of the signal) is:

$$d = 3\lambda \sin \alpha \quad (4.2)$$

Figure 4.5 illustrates equation (4.2). If we regard now a substrate (*s*) with a uniform

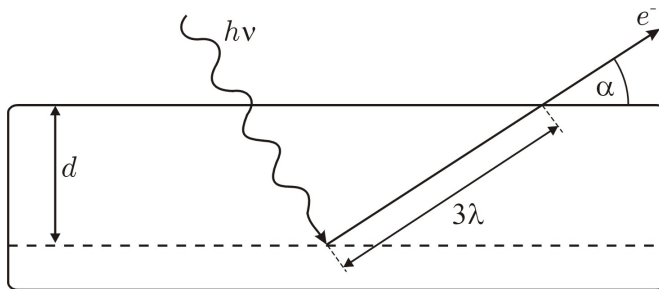


Figure 4.5: 95% of all electrons leaving the sample travel a shorter distance than 3λ before they suffer energy loss due to interactions with the sample. Hence the surface sensitivity can be enhanced by detecting the photoelectrons at a small angle α . The sample distance d from which 95% of the signal originates follows the relation $d = 3\lambda \sin \alpha$.

thin overlayer (*o*) the intensities vary with the angle α as follows [25]:

$$I_s^d = I_s e^{-d/\lambda \sin \alpha} \quad (4.3)$$

$$I_o^d = I_o \left(1 - e^{-d/\lambda \sin \alpha} \right) \quad (4.4)$$

The accuracy of quantitative measurements is claimed to be as low as 5% or 10% if the system is thoroughly calibrated [24]. Although the sensitivity factors can be calculated, there are so many parameters, that usually measuring known reference materials yields more reliable values. Hence the typical error in determining concentrations is 10% to 50%. The lower limit of detectable surface concentration is in the range 1% to 10% of a monolayer [24].

4.3 Infrared Spectroscopy

Infrared spectroscopy is a powerful tool for analyzing chemical bonds. It is widely used in chemistry to identify substances or functional groups of molecules but also quantitative measurements can be conducted [26,27]. Applied to surfaces it can provide information on chemical bonding like the nature of adsorbed molecules, structural properties like bond orientation or bonding site, and electronic and dielectric response with which surface states and adsorbate polarizability can be studied [28]. Infrared spectroscopy, as a vibrational spectroscopy, is based on the absorption of photons within the infrared energy range due to the excitation of molecular vibrations.

4.3.1 Molecular vibrations

In vibrational spectroscopy the wave number $\tilde{\nu}$, which is expressed in cm^{-1} , is a common unit. It counts the number of waves that fit within one centimeter. The fact that $\tilde{\nu}$ is linear with energy makes it a convenient unit. The relationships between wavelength λ , frequency ν and energy E is the following:

$$\tilde{\nu} = \frac{1}{\lambda} = \frac{\nu}{c} \qquad E = h\nu = hc\tilde{\nu} \qquad (4.5)$$

where c is the speed of light (299792458 m/s) and h is Planck's constant (6.626068×10^{-34} Js).

The simplest way in thinking of a molecular vibration is in form of a diatomic harmonic oscillator which is demonstrative and easy to describe mathematically, but in reality the motion of the atoms in a vibrating molecule is anharmonic. The energy levels of a quantum mechanical anharmonic diatomic oscillator can be approximately described as:

$$E_{vib} \approx h\nu_0 \left[\left(n + \frac{1}{2} \right) - x_a \left(n + \frac{1}{2} \right)^2 \right] \qquad (4.6)$$

where x_a is the anharmonicity constant. The energy spacing between two adjacent levels is $E_n - E_{n-1} \approx (1 - 2nx_a)h\nu_0$ and will therefore differ from level to level. The transition

from the ground state ($n = 0$) to the first state ($n = 1$) is called the fundamental transition and as long as $x_a \ll 1$, the energy difference is $\approx h\nu_0$. The horizontal lines in figure 4.6 show the anharmonic energy levels of a diatomic oscillator. The potential curve is a Morse potential of the form

$$V = D_e \left(1 - e^{-a(r-r_e)}\right)^2 \quad (4.7)$$

where r_e is the equilibrium bond length, D_e the dissociation energy of the molecule, and $a = \tilde{\nu}c\sqrt{\frac{\mu}{2D_e}}$ a parameter which controls the width of the potential well. The Morse

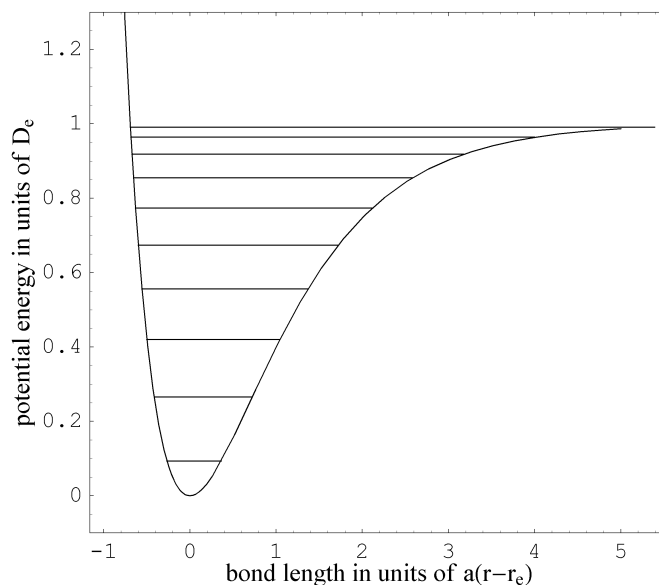


Figure 4.6: Morse potential of the form $V = D_e \left(1 - e^{-a(r-r_e)}\right)^2$, the horizontal lines indicate the energy levels of the anharmonic oscillator $E_{vib} \approx h\nu_0 \left[\left(n + \frac{1}{2}\right) - x_a \left(n + \frac{1}{2}\right)^2 \right]$

potential is often used in spectroscopy, it is a convenient model for the potential energy of a diatomic molecule because it is possible to solve the Schrödinger equation for this system.

The vibration of a polyatomic molecule can be regarded as a system of coupled anharmonic oscillators. A molecule with N atoms has $3N$ degrees of freedom of motion for the nuclear masses. If the pure translation and rotation of the whole molecule are subtracted, there are $(3N - 6)$ degrees of freedom left for nonlinear molecules and

$(3N - 5)$ degrees of freedom for linear molecules. These internal degrees of freedom are normal modes of vibration in which all masses vibrate with the same frequency and pass their equilibrium position at the same time [26]. Since molecules bound to a surface cannot translate or rotate they have $3N$ vibrational degrees of freedom. There are basically two vibration modes, stretching modes in which the atoms move along the direction of the chemical bond and therefore 'stretch' it, and bending modes in which the atoms do not move along the bonding direction but change the angle of the chemical bond, and hence 'bend' it. Bending modes are lower in frequency than stretching modes.

4.3.2 Vibrations induced by infrared radiation

Infrared light is absorbed by a molecule if the frequency of the electromagnetic wave matches the eigenfrequency of the dipole active oscillator. The interaction between the radiation and the vibrating dipole takes place via the electric field of the electromagnetic wave which produces a force on the effective ionic charge of the dipole oscillator. Hence only molecules which have a net dipole moment can be excited and only those vibrations which cause a change of this dipole moment during oscillation can be excited. The intensity I_{ir} of an absorption signal is proportional to the square of the change in the molecular electric dipole moment μ caused by a generalized coordinate q [26]:

$$I_{ir} \propto \left(\frac{\partial \mu}{\partial q} \right)^2 \quad (4.8)$$

The big majority of molecules have infrared absorption signals in the mid-infrared between 400 cm^{-1} and 4000 cm^{-1} . Most of them are from fundamental transitions. Due to the anharmonicity of the vibration, the selection rule $\Delta n = \pm 1$ of transitions between levels of a quantum mechanic harmonic oscillator is weakened. Hence also transitions between non-adjacent levels like, for example $(n = 0) \rightarrow (n = 2)$ are possible. This type of transition is called an overtone transition. The relative intensity of different transitions is the following:

Δn	± 1	± 2	± 3	\dots
rel. intens.	1	x_a	x_a^2	\dots

Since the anharmonicity constant x_a is usually small with respect to 1, the signals from overtone transitions are normally weak compared to fundamental transitions.

For infrared spectroscopy the local electric field at the location of the oscillator is crucial, hence on surfaces the electronic response of the surface layer and any other environment has to be considered. This gives rise to different techniques and sample geometries depending on the sample material and the information one wants to obtain. The macroscopic response of a solid to electromagnetic waves can be expressed by the complex dielectric function $\varepsilon(\nu)$ which is the proportionality factor between the displacement vector \vec{D} and the electric vector \vec{E} .

For metallic surfaces with large values of ε , the components of the electric field parallel to the surface E_x and E_y are small, in the order of $E^0/\sqrt{|\varepsilon|}$, where E^0 is the electric field of the incident beam. For the component perpendicular to the surface E_z the expression $E_z/E^0 \sim 2 \sin \theta$ is valid, where θ is the incident angle with respect to the surface normal. Hence the absorption is dominated by the z -component. Inside the metallic substrate $E_y \approx E_x \sim \sqrt{|\varepsilon|} E_z$, thus the absorption is dominated by the parallel field below the surface. For semiconductors where ε is larger than 10 an important estimation is that all components of the electric field have a similar normalized amplitude of about $2 \cos \theta$ which means one can see every mode [28].

This is used, for example, by internal reflection where the IR beam is injected into the substrate in a way that at the interface total reflection occurs and the beam “bounces” between the two interfaces of the substrate with the surrounding. Therefore the absorption is enhanced. Other techniques or sample geometries, respectively, are external reflection and transmission. Figure 4.7 shows the different sample geometries.

What all these techniques for analysis of adsorbed molecules on surfaces have in common is, that they work with difference spectra. This means a measured spectrum is ratioed against a reference- or background spectrum. Hence the bulk signal is removed

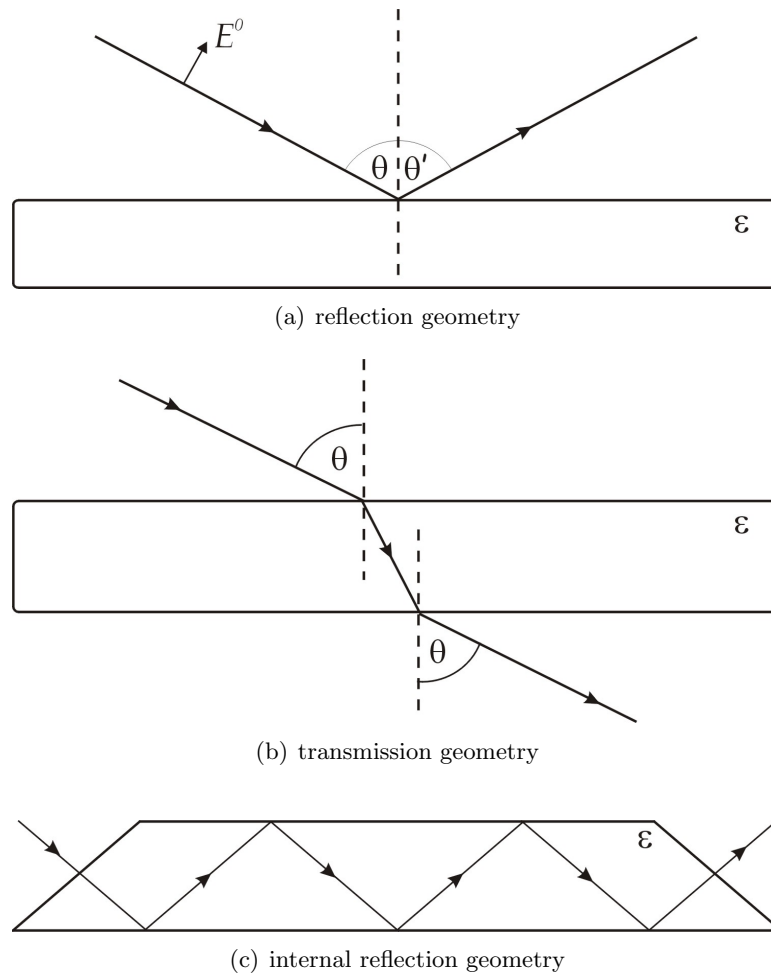


Figure 4.7: In reflection geometry (a) the reflected beam is detected; in transmission geometry (b) the absorbance of the transmitted beam is measured and in internal reflection geometry (c) the beam travels through the substrate and is multiply totally reflected at the interfaces before it exits the substrate. E^0 is the electric vector of the incident beam, $\theta = \theta'$ is the angle of incidence and the angle of reflection, respectively, and ε is the dielectric constant of the substrate.

as well as atmospheric absorptions inside the spectrometer and the instrumental contributions like the characteristics of the source, the response of the beamsplitter, optics, sampling accessory or holder, and detector. But this also implicates that only changes on the sample that occurred between the two measurements can be seen. Since within the bulk nothing should change, the detected changes can be ascribed to changes on the surface.

4.3.3 Fourier Transform Infrared Spectroscopy (FTIR)

There are basically two kinds of infrared spectrometer, dispersive spectrometer and Fourier transform spectrometer (FTIR). The first infrared spectrometer were dispersive instruments (see figure 4.8). In this type of spectrometer, light from an infrared

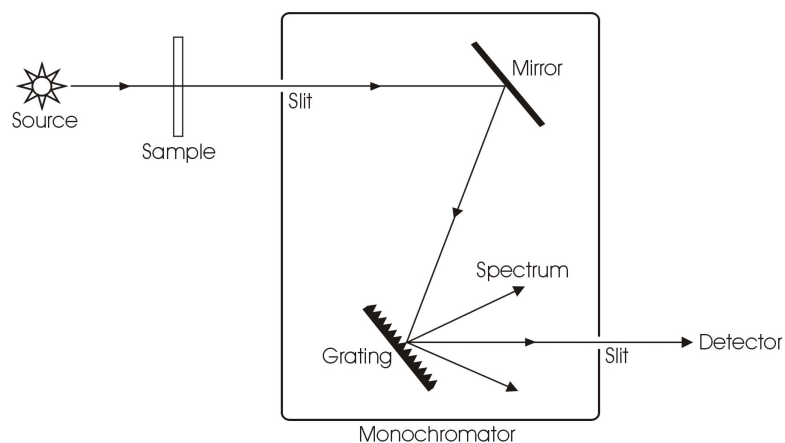


Figure 4.8: The schematic of a dispersive grating infrared spectrometer. The monochromator disperses the light from the sample into a spectrum and selects a narrow band of wavenumbers to strike the detector. (Figure taken from [27])

source passes through the sample and enters a monochromator through a slit. In the monochromator, optics focus the light on a grating or a prism which disperses the light into a spectrum of its wavenumbers. A slit selects a narrow band of wavenumbers to leave the monochromator and strike the detector. By rotating the grating or prism, the spectrum can be scanned. Due to the use of the slit, only a small amount of the total available light energy is able to strike the detector at any given time. The intensity of the light striking the detector is recorded as a function of wavenumber and plotted to

obtain the infrared spectrum. [26]

Fourier transform infrared spectrometers are based on a different functional principle. The light transmitted through or reflected from the sample, respectively, is processed by an interferometer before it strikes the detector (see Figure 4.9). Most

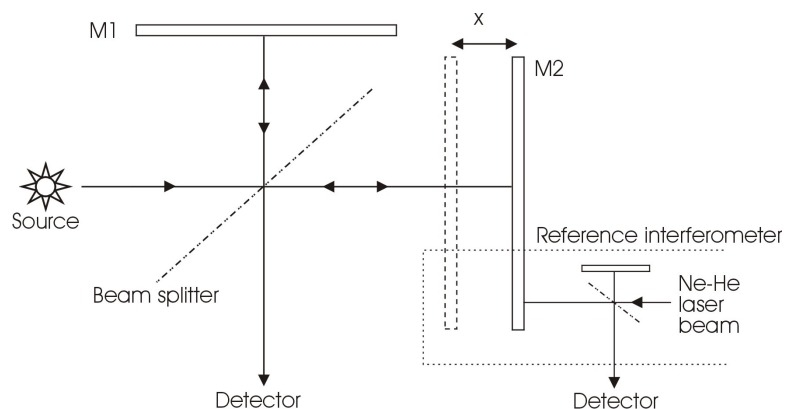


Figure 4.9: The schematic of a Michelson interferometer with a small reference interferometer to precisely control the position of the movable mirror M1. (Figure taken from [26])

FTIRs nowadays contain a two-beam Michelson interferometer [26] which basically consists of a beam splitter, a fixed planar mirror (M1) and a movable planar mirror (M2). M1 and M2 are arranged perpendicular to each other. The beam splitter, a semi-reflective mirror, is placed where the two perpendicular bisectors of the mirrors M1 and M2 intersect and it is aligned in a 45° angle with respect to the mirrors. A beam from the sample is split in two by the beam splitter. The reflected part travels the distance L to the fixed mirror M1, is reflected, travels the same way back and hits the beam splitter after the total path length $2L$. The same thing happens to the transmitted part, but because M2 can be moved very precisely back and forth by a distance x , this part of the beam travels the total path length $2(L + x)$ before it hits the beam splitter again. Thus, when the two parts of the beams recombine at the beam splitter, they have an optical path length difference of $\delta = 2x$. Due to their spatial coherence they interfere on recombination. The radiation that reaches the detector can naturally have only half of the intensity of the radiation entering the interferometer; the other

half is reflected back towards the input.

A general property of waves is that their amplitudes are additive. Thus, if we use a monochromatic light source of wavelength λ , it interferes constructively at path length differences of

$$\delta = n \lambda \quad \text{with} \quad n = 0, 1, 2, 3 \dots \quad (4.9)$$

since the waves are in phase and crest meets crest as well as trough meets trough. They add up and the intensity of the resulting wave is the sum of the intensities of the previous two beams. If the path length difference is an odd multiple of $\lambda/2$,

$$\delta = (2n + 1) \frac{\lambda}{2} \quad \text{with} \quad n = 0, 1, 2, 3 \dots \quad (4.10)$$

the interference is destructive which means crests meet troughs and cancel out. After the interferometer the beam is focused on the detector. The intensity I_D of a monochromatic beam, modulated by the movement of the mirror M2 at the detector is a function of δ and given by the equation [26]

$$I_D(\delta) = \frac{1}{2} S(\tilde{\nu}) [1 + \cos(2\pi\tilde{\nu}\delta)] \quad (4.11)$$

where $S(\tilde{\nu})$ is the intensity of the monochromatic beam with wavenumber $\tilde{\nu}$. Equation (4.11) contains a constant part and a modulated part. For spectroscopic measurements only the modulated part is important. This modulated part is referred to as the interferogram [26]:

$$I(\delta) = S(\tilde{\nu}) \cos(2\pi\tilde{\nu}\delta) \quad (4.12)$$

Since the position of the movable mirror M2 and thus the path length difference δ is a function of time, the interferogram is a function defined in the time domain. If the mirror M2 is scanned at a constant velocity v , the path length difference is $\delta = 2vt$ and thus the interferogram

$$I(t) = S(\tilde{\nu}) \cos(2\pi\tilde{\nu}2vt) \quad (4.13)$$

Therefore, the measured signal oscillates sinusoidally with the frequency

$$f_{\tilde{\nu}} = 2\nu\tilde{\nu} \quad (4.14)$$

If there is light composed of more than one wavenumber, the signal from each component oscillates with a different frequency. Hence the detected signal is a superposition of the signals from the components with different wavenumbers and the intensities add up. For a lightsource with n different wavenumbers, the interference pattern is:

$$I(\delta) = \sum_{i=1}^n S(\tilde{\nu}_i) \cos(2\pi\tilde{\nu}_i 2\delta) \quad (4.15)$$

Since real light sources are *polychromatic* which means the spectrum is continuous, the sum in the interference pattern is replaced by an integral [26]:

$$I(\delta) = \int_0^{\infty} S(\tilde{\nu}) \cos(2\pi\tilde{\nu} 2\delta) d\tilde{\nu} \quad (4.16)$$

here $S(\tilde{\nu})$ is now the spectral power density of the light source. At the optical path length difference $\delta = 0$ all waves, no matter what wavenumber, pass the interferometer. At all other wavenumbers only some will pass, therefore an interferogram has a characteristic “center burst” at zero path length difference and a very complex pattern symmetrically distributed around it.

In order to obtain an interpretable spectrum the interferogram has to be converted from its time domain to the frequency domain. This can be done via a Fourier transformation. The French mathematician and physicist Jean Baptiste Joseph Fourier stated that every function can be described as a composition of sines and cosines with different phases and amplitudes. The conversion between a function and the composition of sines and cosines is called the Fourier transformation. Since an interferogram is a composition of cosines originated from waves with the correspondent wavenumbers, a Fourier transformation can convert it to a spectrum of these wavenumbers. The continuous

Fourier transformation $\mathcal{F}_{t\omega}$ is generally defined as:

$$\mathcal{F}_{t\omega}\{f(t)\} = F(\omega) = \frac{1}{\sqrt{2\pi}} \int_{-\infty}^{\infty} f(t) e^{-i\omega t} dt \quad (4.17)$$

The inverse Fourier transformation $\mathcal{F}_{\omega t}^{-1}$ accordingly:

$$\mathcal{F}_{\omega t}^{-1}\{F(\omega)\} = f(t) = \frac{1}{\sqrt{2\pi}} \int_{-\infty}^{\infty} f(\omega) e^{i\omega t} d\omega \quad (4.18)$$

This transformation applied to our problem results in a spectrum as given by [26]

$$S(\tilde{\nu}) = \int_{-\infty}^{\infty} I(\delta) \cos(2\pi\tilde{\nu}\delta) d\delta \quad (4.19)$$

A detailed derivation of this basic integral of FTIR can be found in “*Introductory Fourier Infrared Spectroscopy*” by R.J. Bell [29]. Equations (4.16) and (4.19) are interconvertible.

Figure 4.10 shows an interferogram of ZnO nanotips on a Si substrate taken with a Thermo Nicolet 6700 FTIR spectrometer. The Fourier transformation of the interferogram from Figure 4.10 results in a “single-beam spectrum” which is shown in Figure 4.11. A single-beam spectrum shows the response at all frequencies in the spectral range. The three most prominent features in this spectrum of ZnO nanotips on a Si substrate are water absorption bands from $\sim 1340\text{cm}^{-1}$ to 2000cm^{-1} and from $\sim 3500\text{cm}^{-1}$ to 3940cm^{-1} and the CO_2 double peak at $\sim 2350\text{cm}^{-1}$. These absorption bands origin from atmospheric water and CO_2 in the spectrometer, not from the sample. In order to get a pure sample spectrum a single-beam spectrum is ratioed against a single-beam background spectrum.

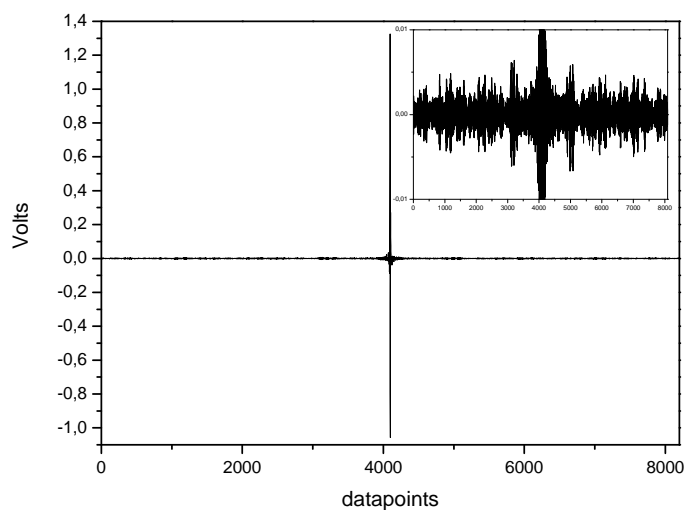


Figure 4.10: Interferogram of ZnO nanotips on Si. The centerburst at datapoint no. 4200 (peak-to-peak value of $\sim 2.38\text{V}$), and the very low intensity of the wings (peak-to-peak value of $\sim 0.02\text{V}$) in comparison to it is clearly visible. The inset shows the same interferogram but with the y-axis magnified by a factor 125 to make the structure of the wings visible. The data were taken with a Thermo Nicolet 6700 FTIR spectrometer.

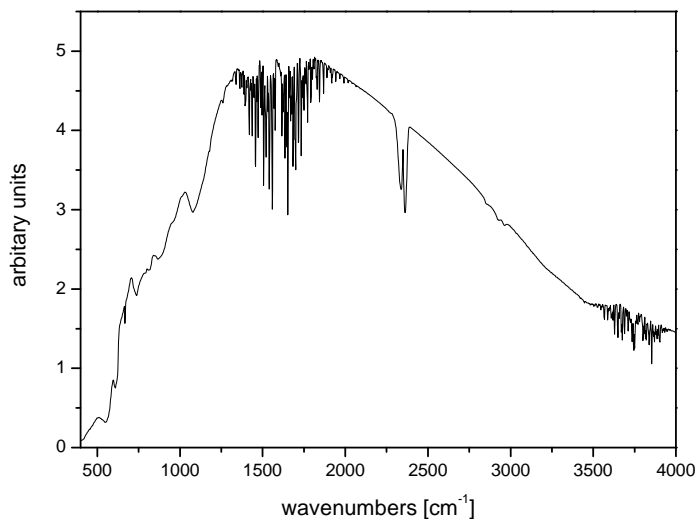


Figure 4.11: Single-beam spectrum of ZnO nanotips after Fourier transformation of the interferogram from Figure 4.10. The three most prominent features are water absorption bands from $\sim 1340\text{cm}^{-1}$ to 2000cm^{-1} and from $\sim 3500\text{cm}^{-1}$ to 3940cm^{-1} and the CO_2 double peak at $\sim 2350\text{cm}^{-1}$. These absorption bands origin from atmospheric water and CO_2 in the spectrometer, not from the sample. The interferogram was Fourier transformed by the software *Omnic* Copyright © 1992-2001 Thermo Nicolet Corporation.

4.3.4 Potential of FTIR

Fourier transform infrared spectroscopy has some advantages in comparison with dispersive spectroscopy techniques. All modern FTIR use a monochromatic He-Ne laser ($\lambda_{He-Ne} = 633 \text{ nm}$ or $\tilde{\nu} = 15800 \text{ cm}^{-1}$) to measure precisely the position of the movable mirror and hence the optical path length difference. This is also done via interferometry (see Figure 4.9). The zero crossing points of the interference signal from the laser are precisely digitized. A zero crossing happens every $\lambda/2$ of the wavelength of the monochromatic laser (see equation (4.12)). Hence the minimum sampling spacing Δx_{min} is $1/31600 \text{ cm}$ or $0.31654 \mu\text{m}$. The error in $\Delta\tilde{\nu}$ is of the same order than the error of Δx which is only determined by the precision of the wavelength of the He-Ne laser. Hence FTIR have a very precise built-in wavenumber calibration. This advantage is called the Connes advantage.

Another advantage is the so-called Jacquinot or throughput advantage. In contrast to dispersive spectrometer, in FTIR all the infrared radiation strikes the detector at once. There are no slits for selection of narrow wavenumber areas which reduce the intensity of IR radiation that strikes the detector. Therefore the maximum amount of light hits the detector at any time during the measurement.

Further, in dispersive spectrometer only a small amount of wavenumbers is measured at a time, in FTIR all wavenumbers are measured at once at any time. Since the noise at a certain wavenumber is proportional to the square root of the time spent observing this wavenumber, the noise in a FTIR spectrum which is measured for a given time is less than the noise in a spectrum measured by a dispersive spectrometer for the same time. Thus, this multiplex- or Fellgett advantage allows to measure much faster or get a better signal-to-noise ratio. [26, 27, 29]

There are two quantities that define the quality of an infrared spectrum, the signal-to-noise ratio SNR and the resolution. SNR is defined by the ratio of the height of a peak and the height of the random fluctuations nearby the peak. The higher the SNR the better. It can be improved by extending the measuring time, since the random fluctuations will average out whereas the signal adds up. Increasing the measuring time

can be achieved by, for example, increasing the number of scans. The relation between SNR, measuring time T and number of scans N , if the velocity of the moving mirror is kept constant during the different scans, can be described as:

$$SNR \propto \sqrt{T} \qquad SNR \propto \sqrt{N} \qquad (4.20)$$

In reality there is a limit of scans after which the SNR will not improve. The reason for this is the fact that not all noise is random and therefore not all noise will cancel out with extended measuring time. Usually a number of 1000 scans is used to get a good SNR. At an optimal SNR the detection sensitivity reaches its maximum but cannot be denounced in a general absolute value, since it depends strongly on the dipole moment of each specific bond.

The resolution of a spectrum can be defined in different ways. The spectral resolution is a measure of the ability of discerning two spectral features that are close together. The smaller the resolution, the better because peaks can be resolved that are closer together. The instrumental resolution is determined by the number of data points in the spectrum. For example in a spectrum with the resolution of 4 cm^{-1} , there is a data point every 4 cm^{-1} . The Rayleigh criterion is a more precise way of defining resolution. It says that two spectral features of equal height are just resolved, if the valley between them has a depth of 20% of the peak height. Another possibility of defining resolution is by the full width at half maximum FWHM. Is there a band with a inherent small line width of, lets say 0.1 cm^{-1} and the peak in the spectrum shows a FWHM of 1 cm^{-1} , the spectrum is said to be taken at a resolution of 1 cm^{-1} [27]. The resolution in FTIR is determined optically by the maximum path length difference δ_{max} and hence by the maximum mirror displacement x_{max} . Imagine two close bands at, e.g. 2000 cm^{-1} and 2001 cm^{-1} . If the mirror is moved only a small amount, only a small amount of the waves of the sinusoids is measured. Since the interferograms of the two close bands look very similar they only can be distinguished if the optical path length difference is big enough. Thus, the relation between resolution and optical path

length difference is:

$$\text{Resolution} \propto \frac{1}{\delta} \quad (4.21)$$

At the center burst, all waves interfere constructively, but in the wings of the interferogram the intensity of the signal decreases very fast. Since the amplitude of the noise is equal all over the interferogram, the contribution to the overall signal is only a few percent at the center burst but much higher in the wings. Hence, the higher the resolution, the more noisy is the spectrum since a longer path length difference causes longer wings in the interferogram.

4.4 Contact angle measurement

There are several ways of measuring contact angles. The most common one for measuring contact angles on flat surfaces is the sessile drop method. It is very straightforward since a drop of water or another liquid is put onto the surface to measure. Then the drop sitting on the surface is viewed from the side and the contact angle is read off either directly with the eye and a goniometer (telescope with an angular scale) or an image is captured electronically by a CCD camera and processed by an image software to determine the contact angle with the aid of a computer. Figure 4.12 shows a view through the telescope of a setup for determining the CA with the eye. In order to get good contrast, to be able to clearly determine the boundaries of the drop, it is highlighted from the backside by a back-light. The indicators in the telescope are a fixed angular scale, a movable scale and a baseline. For a measurement, the base line is aligned with the intersection line of the drop and the sample in the way, that the intersection point of the drop and the sample is placed in the middle of the baseline where the movable scale intersects the baseline. To determine the CA, the movable scale is rotated until it matches the tangent of the drop and thus indicates the contact angle on the angular scale.

The setup for the computer-aided CA measurement is exactly the same but with the telescope replaced by a CCD-camera which is connected to a PC with the CA

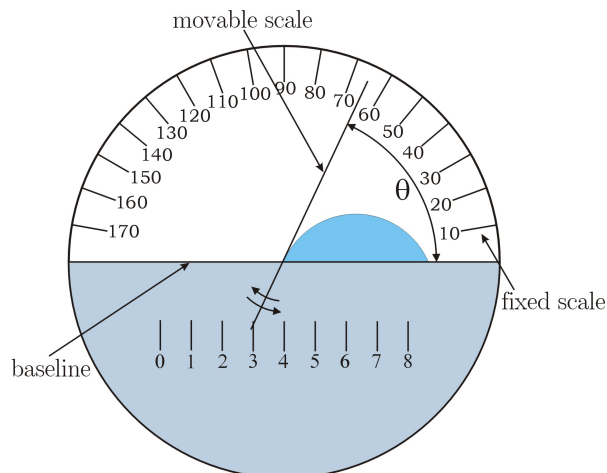


Figure 4.12: View through the telescope of a contact angle goniometer. The drop is aligned with the baseline and the intersection point of the movable scale and the baseline. For CA measurement, the movable scale is rotated until it matches the tangent to the drop and thus indicates the CA on the fixed scale.

measurement software installed (see Figure 4.13). For this thesis we used a computer-

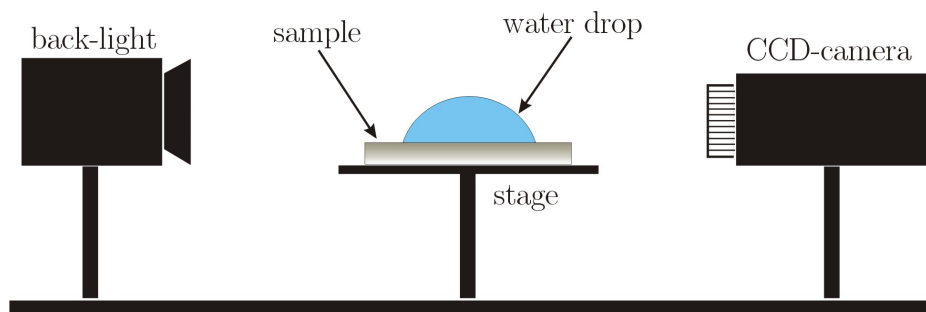


Figure 4.13: Setup for computer-aided CA measurements. The sample with the drop on it is highlighted by a back-light to provide a good image quality and contrast. The CCD-camera captures a picture from the side view and sends it to the connected PC with installed CA measurement software which processes the image and determines the contact angle.

aided system. It is the *Model 500 Advanced Goniometer* from ramé-hart instrument co.. The software we used is the “DROPimage Advanced Software; a program system for interfacial tension and contact angle measurement by image analysis; Advanced Edition” by Finn Knut Hansen, which was delivered with the goniometer. The program has several routines implemented for measuring contact angles, from fitting a theoretical

drop profile as part of a interfacial tension calculation to pure numerical methods. The method we used is a numerical method in which a horizontal line on the screen is aligned with the solid surface of the sample. A properly aligned drop profile is then given by a filter routine. The contact angle is simply calculated by numerical derivation of the profile at the contact point of water and solid [30]. The software always calculates the contact angles on both sides of the drop on the image and shows both values as well as the average value of them.

Chapter 5

Experimental results and discussion

Zinc oxide has many interesting properties, one of them is its sensitivity to light and its photocatalytic properties [31, 32]. But exposing ZnO to light does not only control its catalytic properties but also can influence its wettability. If a hydrophobic ZnO surface is irradiated with UV light it changes its wetting properties to hydrophilic, in other words from a high contact angle to a low contact angle. This wettability change is reversible by storing the ZnO sample in the dark for a certain amount of time. The contact angle change on an array of ZnO nanotips induced by UV irradiation and its reversibility is investigated within this thesis by means of contact angle measurements, FTIR and XPS. The essential question is, can we gain insights into the mechanisms of wettability at the atomic level, using surface-sensitive spectroscopic methods?

5.1 Control of contact angle changes

5.1.1 Contact angle procedures

As described in section 4.4, the contact angle measurement was conducted by means of the computer aided CA measurement system *Model 500 Advanced Goniometer* from ramé-hart instrument company. For a CA measurement a small drop of DI water is put onto the sample surface via the automated dispenser system from ramé-hart. Then an image is captured from the side view with a CCD camera and processed by an image analysis software which calculates the contact angle. The automated dispenser system is a software driven dispenser tool with which the drop volume can be precisely controlled. The usual drop volume we used was $5\mu\text{l}$.

The procedure for placing the drop is to approach the surface of the sample with the

tip of the syringe, which is connected to the automated dispenser system. Then a drop of a defined volume (e.g. $5\mu\text{l}$) is formed at the tip of the syringe by the dispenser. The syringe with the drop on its tip is now approached to the surface until the water touches it. When the contact is established, the syringe is drawn back and the drop stays on the surface, relaxing to its equilibrium shape and position. Ideally this equilibrium shape is symmetric and the CA is the same all along the contact line. In reality this is not always the case. Due to inhomogeneities of the surface the CA can vary around the contact line of the drop with the surface. To minimize the uncertainties in the CA measurements and to improve the reproducibility of the CA results, we took data only from drops of a symmetric shape and took the average value between left and right contact angle on the captured image. The values between left and right CA could still differ by about two to three degrees. Hence, although the measurement and the calculation itself is accurate to about 0.1° , the CA for a given surface can be determined only by an accuracy of $\pm 2^\circ$. Figure 5.1 shows typical images taken during CA measurements.



Figure 5.1: Images of drops taken during CA measurements (a) $CA \sim 107^\circ$, (b) $CA \sim 8^\circ$. Since these images, taken by the CCD camera of the CA goniometer, were actually used by the software to determine the CA, the contrast is very high so that only the shape is visible and the drops are not distinguishable from the surface material.

5.1.2 Contact angle measurements

Non-doped ZnO nanotips grown on Si substrates show the following wetting properties. Directly after the growth, the fresh ZnO nanotips surface is hydrophilic with a low

CA of about 20° . If stored in the dark in a nitrogen box at room temperature the CA rises slowly until it reaches a maximum value of 100° to 110° . This transition to the hydrophobic state takes one to two months to reach the maximum CA value if no special treatment is applied. If this hydrophobic ZnO nanotip surface is irradiated with UV light, the CA decreases quickly to very low values of down to under 5° , depending on the sample, irradiation time and power output of the UV lamp. This cycle: low CA \rightarrow dark storage \rightarrow high CA \rightarrow UV irradiation \rightarrow low CA \rightarrow dark storage \rightarrow high CA... is repeatable (see also Figure 5.2).

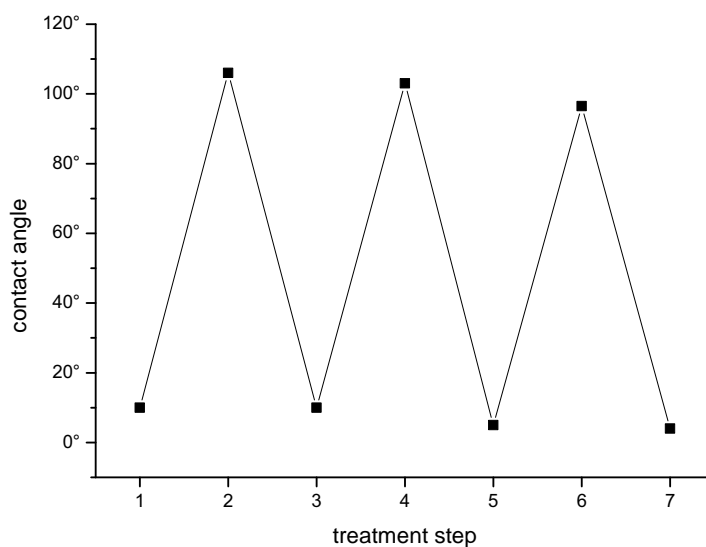


Figure 5.2: CAs at corresponding sample treatment steps in the cycle: low CA \rightarrow dark storage \rightarrow high CA \rightarrow UV irradiation \rightarrow low CA \rightarrow dark storage \rightarrow high CA ...; the dark storage time in this cycle was decreased: the sample was stored for 20h at 50°C with oxygen flow.

For irradiating the samples with UV light we used two different lamps. The first lamp was a Model B-100A Hi Intensity UV Lamp from UVP, Inc. It is a long wavelength Hg UV lamp with a 100W bulb and emission peak at $\lambda = 365$ nm. The manufacturer's specification of the intensity is $21700/8900$ [$\mu\text{W}/\text{cm}^2$] at 2 in/10 in. We measured the intensity at the position of the sample with the aid of a Si photo-detector from Oriel; the distance to the lamp was about 10". The response of the detector in the wavelength range from 200 nm to 400 nm is 0.12 A/W, the resistance is 10k Ω . With a measured

voltage of 2.4V and a detector area of 1cm^2 the intensity is:

$$I = \frac{2.4V}{10^4\Omega \cdot 0.12\frac{A}{W} \cdot 1\text{cm}^2} = 2 \times 10^{-3} \frac{W}{\text{cm}^2} \quad (5.1)$$

and hence smaller than the specifications. For a CA change from $\sim 100^\circ$ to $\sim 10^\circ$ at a distance between lamp and sample of approximately $10''$ it takes about 15-20 min of UV irradiation with the Model B-100A. Figure 5.3 shows a plot of measured CAs as a function of UV irradiation time. The black line is an exponential decay fit of

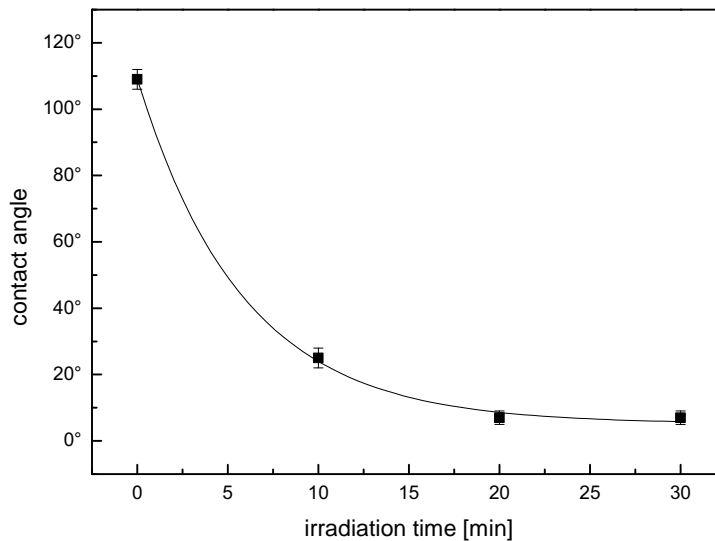


Figure 5.3: Contact angle of a water drop on a ZnO nanotip surface grown on Si as a function of irradiation time with the UV lamp model B-100A. The black line is an exponential decay fit of first order $y(x) = a \cdot \exp(-\frac{x}{\tau}) + y_0$.

first order $y(x) = a \cdot \exp(-\frac{x}{\tau}) + y_0$ with the fitted parameters $a = (103.87 \pm 0.69)^\circ$, $\tau = (5.84 \pm 3.50)$ min and $y_0 = (5.22 \pm 1.91)^\circ$. This experiment was done with two different samples from different growths, but the measured data was exactly the same for both experiments.

The second lamp we used was an Osram XBO 150W/4 Xe UV short arc lamp in a housing and a power supply from Oriel. Xe short arc lamps emit a spectrum close to daylight spectrum (see Figure 5.4). In order to get mostly UV radiation we used a

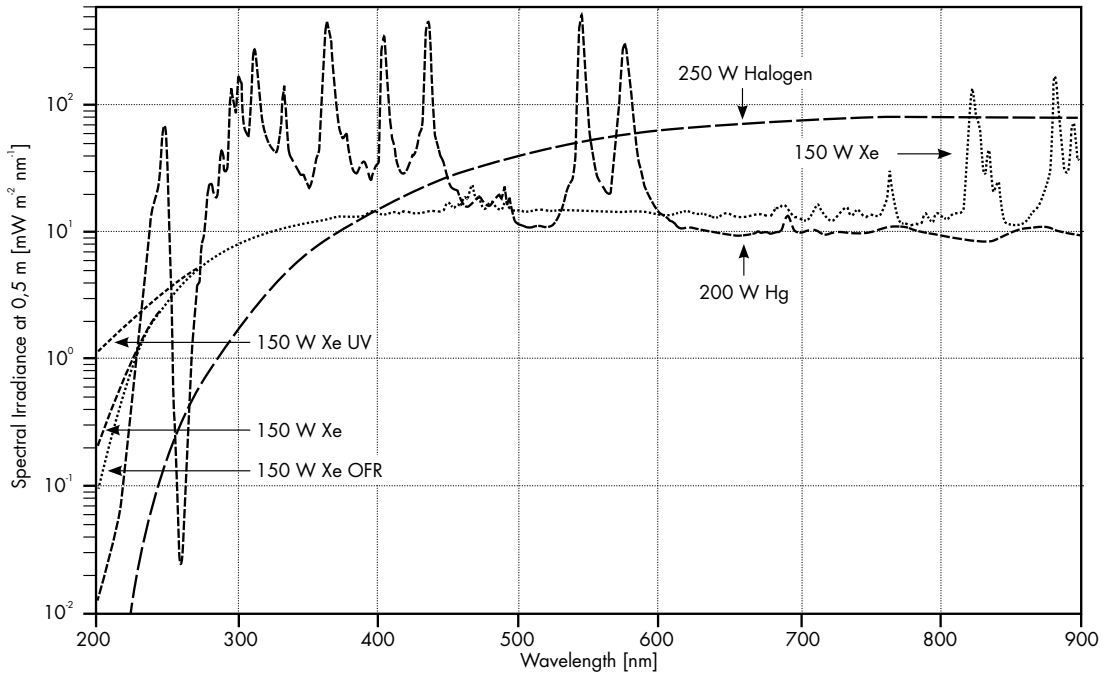


Figure 5.4: Lamp spectra of different arc lamps. (taken from [33])

bandpass filter that transmits mainly in the wavelength range from 250 nm to 390 nm. Figure 5.5 shows a measured transmittance spectrum of the filter used. We operated the lamp at 120W. The intensity of the radiation after the filter at the sample position was measured with the Si-photodetector from Oriel. The detected voltage was 4.3V, hence the intensity is approximately $3.6 \times 10^{-3} \text{W/cm}^2$. The average irradiation time with this setup necessary to decrease the CA of an undoped ZnO nanotip surface grown on Si from $\sim 100^\circ$ to $\sim 10^\circ$ is about 5-10 min which is consistent with the 15-20 min of the other lamp with the accordingly lower intensity.

5.1.3 Minimization of the transition time low \rightarrow high CA

The time for a wettability change from hydrophilic to hydrophobic by means of dark storage is very long compared to the transition from hydrophobic to hydrophilic induced by UV radiation. Therefore we varied the environmental conditions during the dark storage to find a possible way to minimize the transition time without directly affecting the surface like, for example, with chemical treatments. The fastest transition was

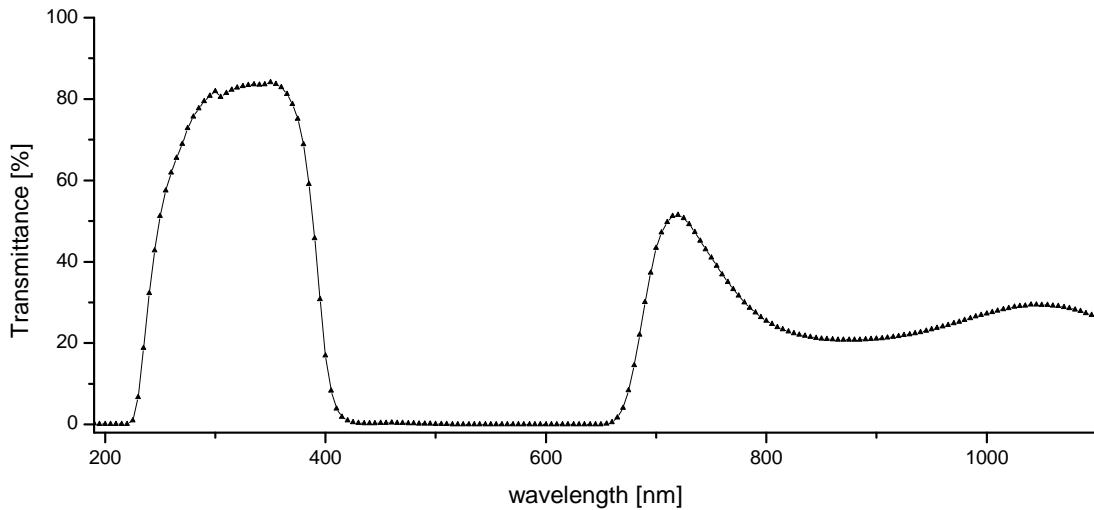


Figure 5.5: Measured transmittance spectrum of the used filter.

achieved by storing the samples in a chamber with oxygen flow at a temperature of 50°C . A Si sample covered with ZnO nanotips with a low CA of under 10° recovers to a high contact angle of over 100° within 20 hours. This is an enormous improvement in comparison with the month necessary for recovery by dark storage in a nitrogen box at room temperature. But also, in comparison with published recovery times of at least 6 to 7 days measured on ZnO films as well as on ZnO nanotips [34,35] the time is shortened by a factor 6. Increasing the temperature will not additionally shorten the recovery time but will have the opposite effect since after a heat treatment with temperatures of over 100°C the ZnO sample becomes hydrophilic. One sample we treated with 200°C became permanently hydrophilic ($\text{CA}\approx 30^{\circ}$). ZnO nanotips on substrates other than Si show similar behavior as long as the surface morphology is the same.

5.1.4 CA hysteresis

Another interesting property of our ZnO nanotip surfaces is the strong hysteresis of the CAs. The difference between the static CA of a drop placed on the surface with the method described above and an advancing CA is often $>40^{\circ}$. one ZnO nanotip surface with an advancing CA of 115° had a receding CA of 15° so the hysteresis is even 100° in that case. All measured samples had strong hysteresis but the value was not always the

same. There were no systematics observed. Measuring advancing CA was conducted by placing the drop on the surface and increasing the volume of the drop by adding water with the syringe until the contact line with the solid starts to move. The movement is not continuous but more like little “jumps” back to the static CA when the threshold of a maximum advancing CA is reached. This could be explained by the water molecules on the surface of the solid sitting in some sort of energy minimum and hence they have to overcome the potential well in order to be moved. Therefore this great hysteresis of the CAs is the reason why water drops on ZnO nanotips don’t move easily but stick to the position they were placed. The sticking is so strong that a drop of $10\mu\text{l}$ with a high CA of 100° does not move even if the sample is brought into a vertical position or even upside down. The receding CA is measured the same way as the advancing one but by decreasing the drop volume; the syringe is used to “suck” water from the drop. Figure 5.6 shows an image of a drop with syringe taken during measurement of a receding CA of 15° .

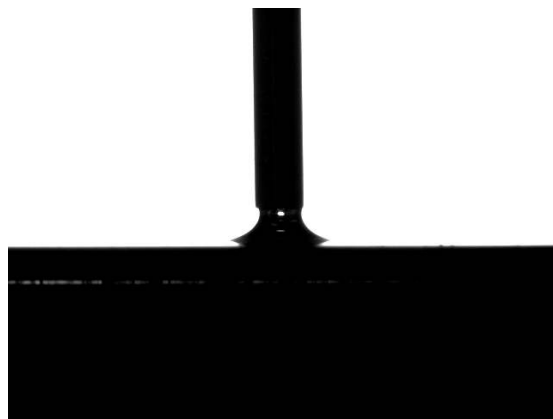


Figure 5.6: Image of a drop with syringe taken during measurement of a receding CA. The receding CA in that case is 15° .

5.1.5 Flat films and N-doping

Contact angle measurements on flat ZnO films and N-doped ZnO nanostructures showed the influence of the surface morphology on the CA. Figure 5.7 shows SEM images of a flat ZnO film grown on r-sapphire and N-doped ZnO nanostructures grown on Si. On

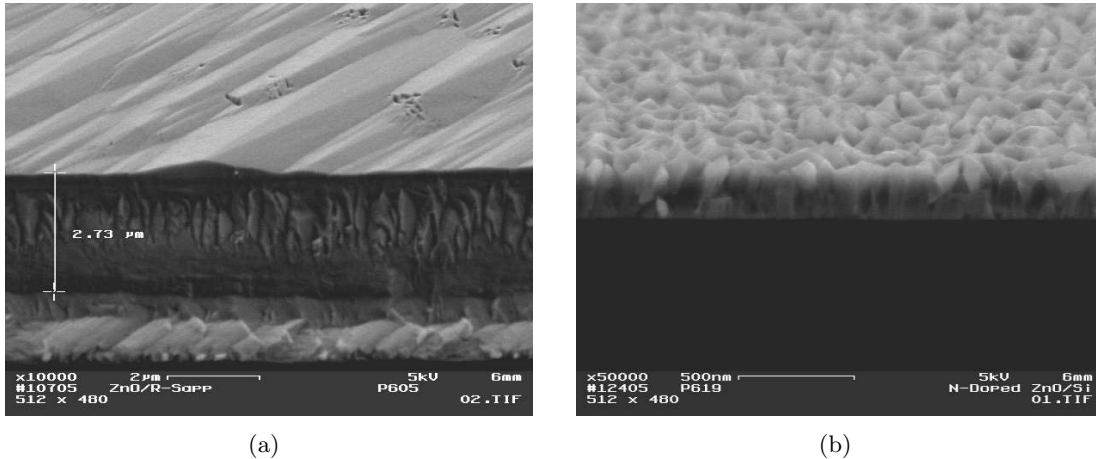


Figure 5.7: SEM images of (a) flat ZnO film grown on r-sapphire and (b) N-doped ZnO nanostructures grown on Si.

flat films (Figure 5.7(a)), the lowest CA after UV irradiation we measured was $\sim 45^\circ$, the highest CA $\sim 90^\circ$. This result was expected since the surface roughness has an amplifying effect on both hydrophobicity and hydrophilicity as described in chapter 2. The nitrogen doping of ZnO grown on Si affects the morphology of the surface. ZnO does not grow in slender separated nanotips like undoped ZnO but more in a rough disordered hill and valley structure as seen in Figure 5.7(b). The measured minimum and maximum CA were 40° and 120° , respectively. Further N-doped ZnO surfaces recover faster to high CAs but are less sensitive to UV light. After UV irradiation with the Model B-100A Hi Intensity UV Lamp for over 30 min the CA decreases from about 110° only to about 80° .

5.2 XPS measurements

In order to get a better understanding of the wettability change of ZnO surfaces, we used x-ray photoelectron spectroscopy to identify the atomic species on the surface as well as their atomic concentrations and chemical shifts.

5.2.1 Systems used

One of the two XPS systems I used is a Kratos Model 800. Figure 5.8 shows a scheme of the used configuration. It consists of three separate chambers. The main chamber where

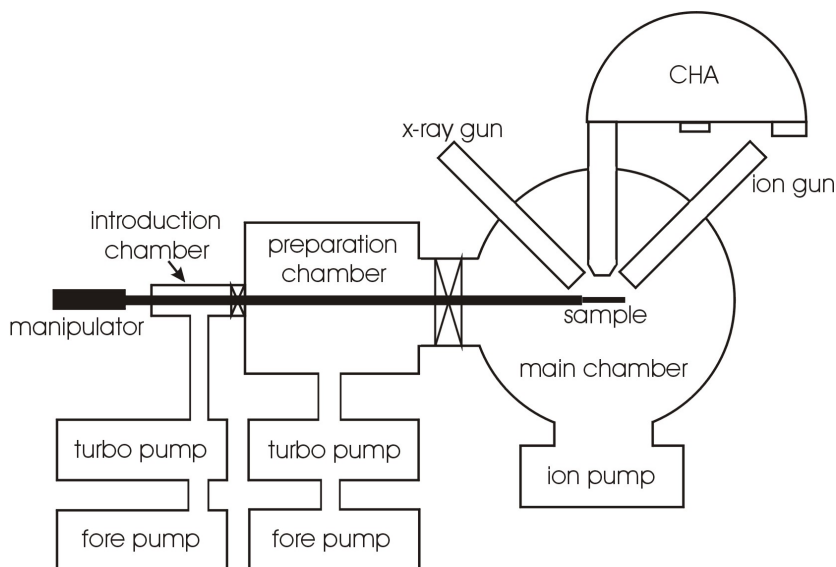


Figure 5.8: Scheme of the XPS system Kratos.

the measurements are actually done contains a x-ray gun, a concentric hemispherical analyzer (CHA) and an ion gun for sputtering. It is connected to the “preparation chamber” where some sample preparations could be done; I used it only as intermediate chamber to keep the vacuum high in the main chamber during pumping when a sample was introduced into the system. The connection between main and preparation chamber can be closed by a valve. The last chamber, which is separated from the preparation chamber by another valve, is an introduction chamber with a small volume to keep the pumping time low when a sample is introduced into the system. The main chamber is pumped by an ion pump; each of the other two chambers is pumped by a turbo pump with a mechanical pump as fore pump. The base pressure of the main chamber is 2×10^{-9} torr; during XPS measurements the pressure was usually between 6×10^{-9} torr to 1×10^{-8} torr.

For introduction of a sample into the system it is attached with carbon tape onto

the sample holder which is attached to the manipulator. The manipulator is introduced into the introduction chamber which is then pumped down with the turbo pump for 20 min before the valve to the preparation chamber is opened and the manipulator is pushed further. In this position in the preparation chamber it stays for at least two hours to pump it down to less than 5×10^{-8} torr. When this pressure is reached the valve to the main chamber can be opened and the sample be pushed into the measuring position. Since the manipulator consists of a smooth rod, the sample can be rotated around its axis to vary the sample angle with respect to the electron analyzer.

The second XPS system we used is a modified system from Φ *Physical Electronics*. It consists of a main chamber which contains a x-ray gun and a CHA, and a smaller introduction chamber with a load lock that consists of a lock that is sealed with a Viton ring. The main chamber is pumped via an ion pump, the introduction chamber via a turbo pump with a mechanical pump as fore pump. Figure 5.9 shows a schematic of the system. The base pressure of the main chamber is $\approx 10^{-9}$ torr, the pressure during

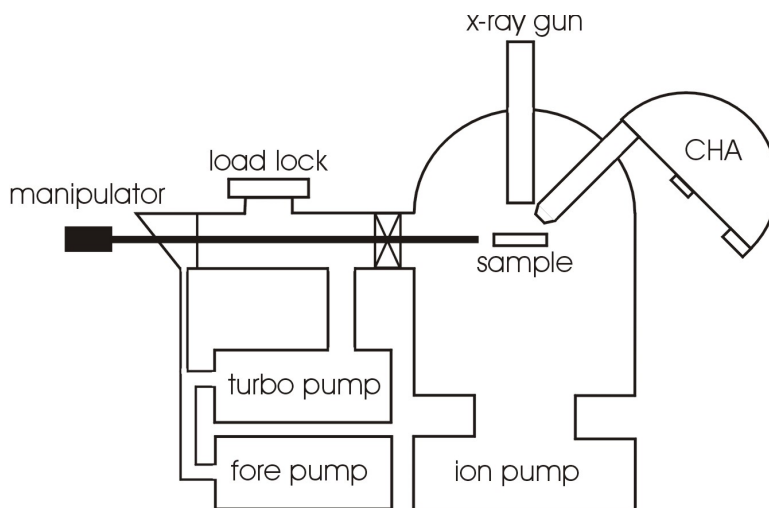


Figure 5.9: Scheme of the modified XPS system from Φ *Physical Electronics*.

measurements was about 7×10^{-9} torr. The loading time on this system is also about two hours. In contrast to the Kratos system the manipulator just transfers the sample to a fixed sample stage; and is pulled back into the introduction chamber to be able to close the valve to the main chamber for a better vacuum. In this system the sample

angle with respect to the electron analyzer is fixed at 45° .

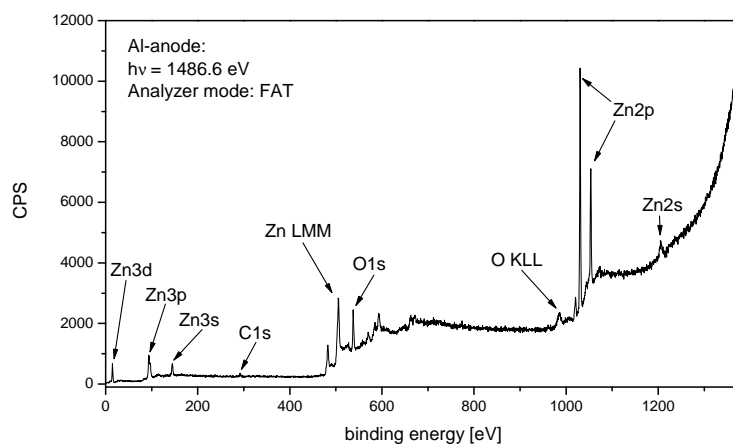
5.2.2 Measurements

In a typical measurement cycle, a survey scan is measured initially. To be able to identify which atomic species are present on the surface, this is a scan over the whole energy range where peaks of interest could be. Figure 5.10 shows three survey scans of ZnO nanotips with different analyzer modes and photon energy. Figure 5.10(a) is a survey spectrum taken with AlK_α radiation ($h\nu = 1486.6$ eV) and fixed analyzer transmission (FAT) as analyzer mode. The pass energy is 17.5 eV, the step width is 0.4 eV and the time per step is 150 ms. The identified core-level peaks are indicated in the graph; Table 5.1 contains the associated peak positions. No doublet is resolved

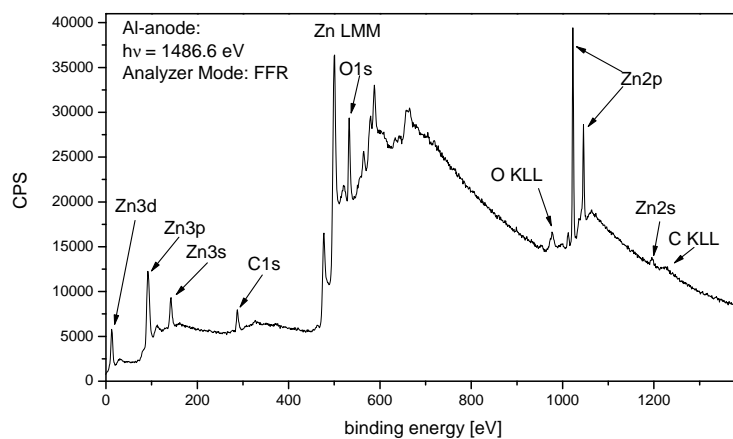
core level	Zn3d	Zn3p	Zn3s	C1s	O1s	Zn2p _{3/2}	Zn2p _{1/2}	Zn2s
position [eV]	12	92	142	287	532	1022	1045	1196

Table 5.1: Core level peak positions in a survey scan of ZnO nanotips.

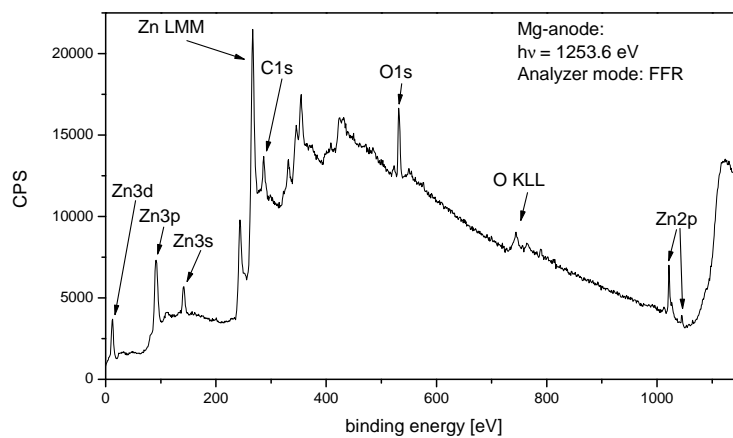
except that of Zn2p. Figure 5.10(b) also shows a survey scan with AlK_α radiation but with fixed retarding ratio (FRR) as analyzer mode. The retarding ratio is 5, the energy step width is 1 eV and the time per step is 130 ms. It is clearly visible that the peak positions are the same but the intensity is different. With respect to FAT the lower binding energy peaks are enhanced. Hence, for identifying peaks I usually used FRR since the peaks are more visible due to the analyzer transmission properties. For quantitative analysis however FAT is used, hence all detailed spectra are taken with FAT. In order to distinguish core level peaks from Auger features I also used MgK_α radiation. The kinetic energy of Auger electrons is independent of the exciting photon energy. Since the binding energy scale is calibrated for the core level peak positions, the Auger features are shifted by the difference of the photon energies used. Hence if survey spectra taken with AlK_α and MgK_α are compared to each other, all core level peak position stay the same on the binding energy scale but all Auger features are shifted by 233 eV, the energy difference of the exciting photons. Figure 5.10(c) shows a survey scan with MgK_α radiation and FFR. The retarding ratio is 5, the energy step width



(a)



(b)

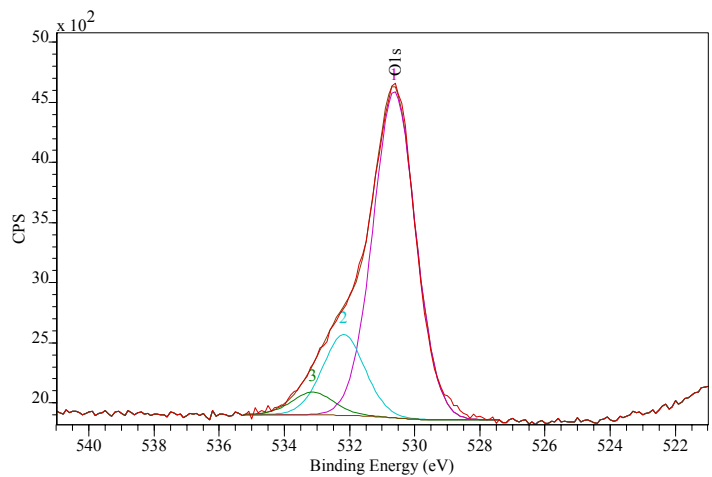


(c)

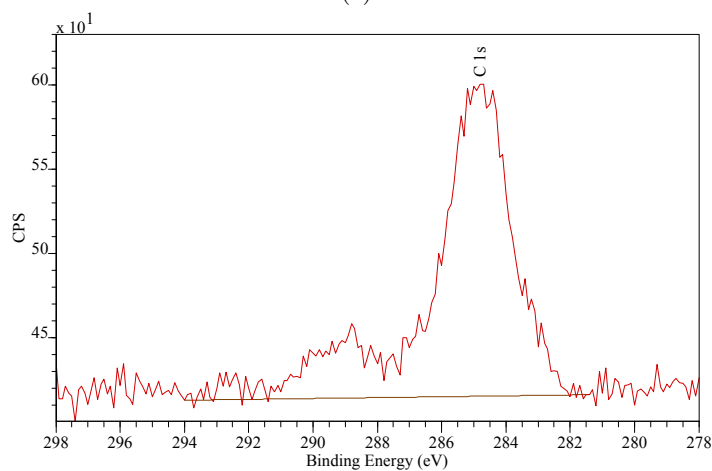
Figure 5.10: XPS survey spectra of ZnO nanotips. (a) analyzer mode: FAT, Al-anode; (b) analyzer mode: FFR, Al-anode; (c) analyzer mode: FFR, Mg-anode.

is 1 eV and the time per step is 130 ms. The different relative peak positions between core levels and Auger features are clearly visible. The feature at high binding energies, starting at 1060 eV is an artifact from the electron analyzer.

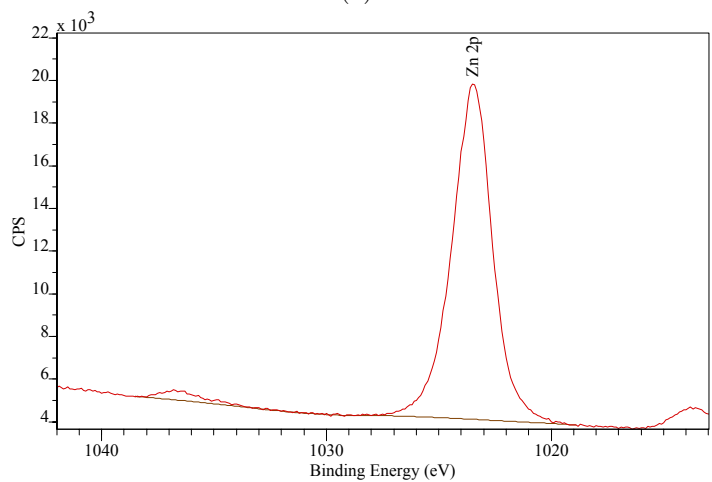
When all peaks are identified and more information like the peak-shape, exact line positions or quantitative informations shall be investigated, a detail scan of the according binding energy area with a better resolution is carried out. The energy step width for detail scans is on both systems 0.1 eV, the analyzer mode is FAT with the pass energy set to 20 eV for the Kratos system and 17.5 eV for the Φ system. Figure 5.11 shows detail scans of the O1s, C1s and Zn2p_{3/2} peak of a ZnO nanotip surface taken with the Φ system under a electron take off angle of 45°. In the detail scans the binding energy decreases from left to right which is common for XPS spectra. All binding energy scales are calibrated with respect to the C1s peak position which is assumed to be at a binding energy of 284.8 eV. The O1s peak in Figure 5.11(a) is at the position 530.6 eV and has a distinct shoulder at the higher binding energy side. This peak shape can be fitted with three peaks which are usually ascribed to O–Zn, Zn–OH and a third component which is sometimes ascribed to H₂O [34, 36, 37]. The fit was done with the two constraints of all peaks having the same FWHM and defined relative peak positions. The relative peak positions were determined by averaging all best fits of several O1s scans I made. So the height of all peaks and the FWHM as well as the position of the first peak was adjusted by the fitting routine which allows an objective comparison of the peak areas in order to detect concentration changes of the three states. The relative peak positions were $a+1.55$ eV and $a+2.5$ eV with a being the position of the first peak. The FWHM of the fitted O1s components is 1.49 eV. In order to get a good signal to noise ratio (SNR) the spectrum is an accumulation of 50 scans. Since it is used as reference, the C1s peak from Figure 5.11(b) is set to the position 284.8 eV. It has a FWHM of 2.1 eV. The cross section for C1s electrons to be excited by x-rays at the used energy is quite low, hence the signal is weak and in order to get a reasonable SNR, 75 scans were accumulated for this spectrum. The Zn2p_{3/2} signal in contrast is relatively high, so only 30 scans were used to get a good SNR. Figure 5.11(c) shows this symmetric peak at the position 1023.5 eV with a FWHM of



(a)



(b)



(c)

Figure 5.11: Detail scans of the (a) O1s, (b) C1s and (c) Zn2p_{3/2} peaks of a ZnO nanotip surface. In this illustration the binding energy decreases from left to right! The spectra are taken with the Φ system under a electron take off angle of 45°

1.89 eV.

5.2.3 Quantitative measurements

For investigating the mechanisms causing the CA change it is not only important to know what species are present on the surface but also their concentration. As described in chapter 4.2.5, XPS can also give quantitative informations about the relative atomic concentration of the detected elements. The peak areas are direct proportional to the number of detected atoms and if divided by a “relative sensitivity factor” (RSF) the peak areas of different elements are comparable, hence the atomic concentration (at%) can be evaluated. The RSFs I used were given by the operating software of the Kratos system, 0.25 for C1s, 0.66 for O1s and 7.2 for Zn2p_{3/2}. For the Φ system I used the same RSFs except for Zn2p_{3/2} which had to be adjusted to 5.3 in order to get comparable results. The ratio of zinc to oxygen, calculated by the areas of the Zn2p_{3/2} peak and the fitted O1s peak ascribed to O–Zn, is (1.03 ± 0.03) .

In order to find correlations between different contact angles and according changes of species on the surface and their concentrations, we measured ZnO nanotips samples with different CAs. Since we expected to see the largest changes in the XPS measurements, we mainly compared samples with very low CA directly after UV shining and very high CA after a long storage time or heating treatment at 50°C for 20h. Figure 5.12 shows a plot of the fitted components of the O1s peak as functions of the CA. The measurements were carried out under a sample angle of 45° with respect to the electron analyzer. Data from both XPS systems are included. The peak areas are normalized by the overall O1s signal. The data of the O–Zn ascribed component (■) are scattered around 75%, the O–H ascribed component (●) around 19% and the third component (▲) around 6%. *Within the experimental error no correlation of the O1s components with the measured CAs can be found.*

Therefore we could not reproduce the results from Ren-De Sun et.al. [34] who measured an increase of the O–H ascribed and the third component, which they ascribed to H₂O, with decreasing CA. They proposed a mechanism of the wettability change

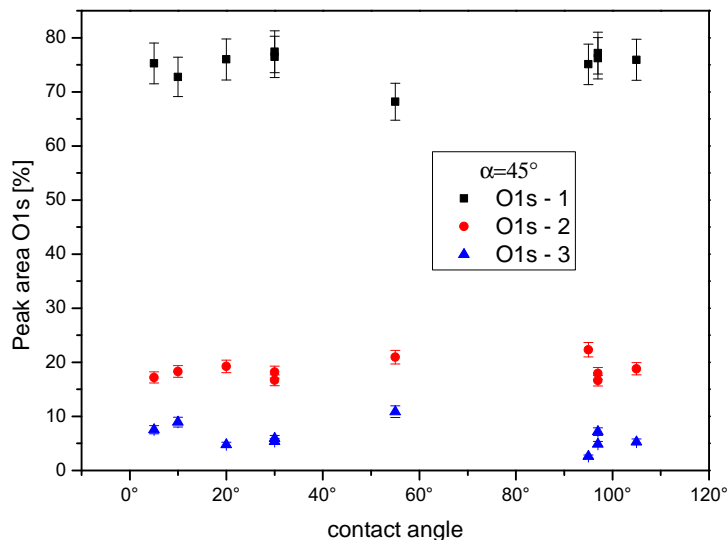


Figure 5.12: Plot of the fitted components of the O1s peaks as functions of the CA before the XPS measurement. The peak areas are normalized by the overall O1s signal. The O1s-1 data points (■) are attributed to O-Zn, O1s-2 (●) to O-H and O1s-3 (▲) to a third component. The measurements were carried out under a sample angle of 45°; there are data from both XPS systems included.

based on creation and healing of oxygen vacancies. They state that UV irradiation creates electron-hole pairs where the holes react with lattice oxygen to form oxygen vacancies on which water adsorbs dissociatively, which leads to a hydrophilic surface. The recovery from low to high CAs during dark storage is said to occur by replacing the adsorbed OH groups by oxygen atoms which is thermodynamically more favorable.

Although the data of Figure 5.12 were taken under a grazing angle of 45° they are less surface sensitive than data taken at a 90° sample angle. Figure 5.13 illustrates the inverse surface sensitivity enhancement of a nanotip surface due to the surface geometry. Although our real surface structure is not quite as simple, this inverse surface sensitivity enhancement is also reflected in the measured XPS data. The C1s signal as well as the two shoulder components of the O1s signal increase with changing the sample angle from 45° to 90°. This means that the measured carbon atoms as well as OH and the third fitted component of the O1s peak are located on the surface and not within the bulk. Figure 5.14 shows an O1s peak measured with the Kratos system under a sample

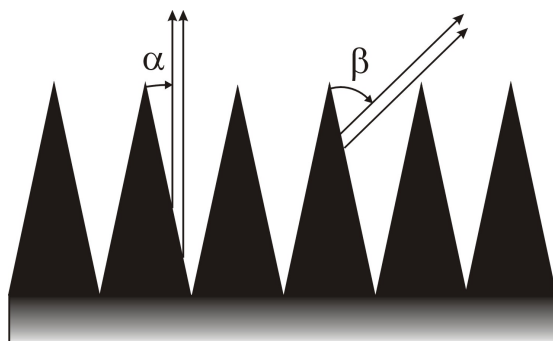


Figure 5.13: Effect of inverted surface sensitivity enhancement on nanotip surfaces. The real take off angle (α) at a sample angle of 90° is smaller than the real take off angle (β) at a sample angle of 45° .

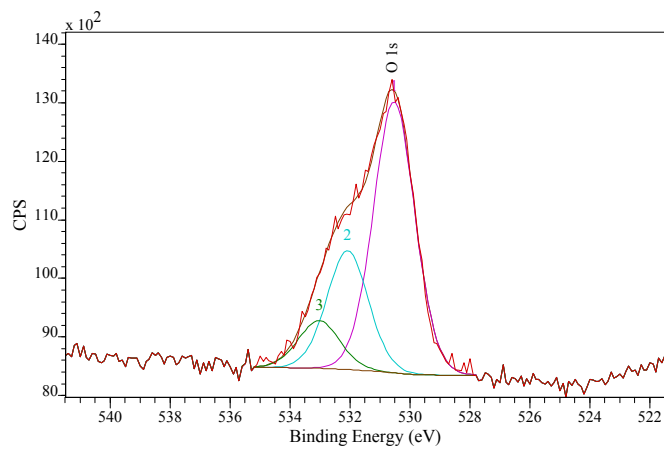


Figure 5.14: O1s peak measured with the Kratos system under a sample angle of 90° . The shoulder components are increased in comparison with a sample angle of 45° (see Figure 5.11(a)).

angle of 90° . The increased shoulder with respect to a sample angle of 45° (see Figure 5.11(a)) is clearly visible. The spectra measured with the Kratos system under a sample angle of 45° were also measured under a sample angle of 90° . Figure 5.15 shows the results of the O1s peaks with the fitted components. Also in this more surface sensitive

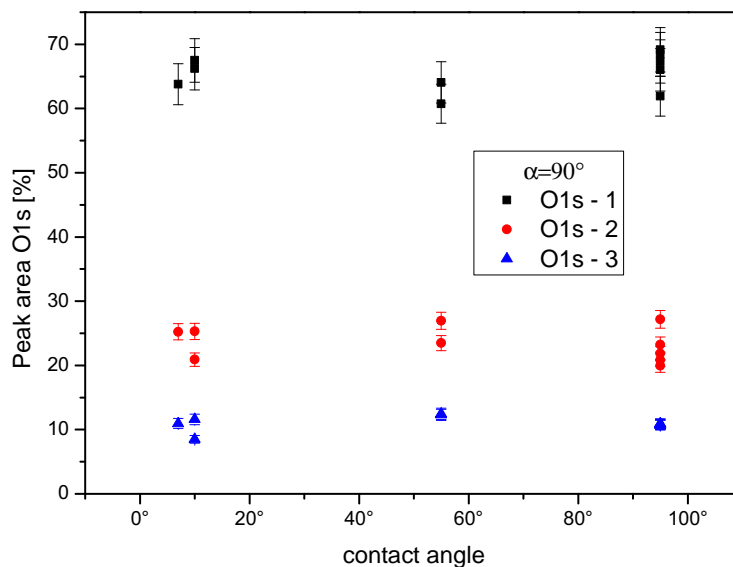


Figure 5.15: Plot of the fitted components of the O1s peaks as functions of the CA before the XPS measurement. The peak areas are normalized by the overall O1s signal. The O1s-1 data points (■) are attributed to O-Zn, O1s-2 (●) to O-H and O1s-3 (▲) to a third component. The measurements were conducted under a sample angle of 90° with the Kratos system.

mode there is no correlation visible between CAs and peak areas of the O1s components. The O-Zn component (■) is scattered around 65%, the O-H component (●) around 24% and the third component (▲) around 11%.

5.2.4 Carbon contamination

All contact angles mentioned so far have been measured before introducing the samples into the vacuum systems for XPS measurements. We observed the fact, that the CA of samples with low CAs before XPS measurements is increased after the measurements. The CA enlargement could be as high as 95° , for example, from 5° before the

measurement to 100° after the measurement. In order to exclude possibilities of CA changes due to the measurement itself we introduced samples with low CA into the Kratos vacuum system without measuring at all, pumped down to 10^{-8} torr for about 30 min, and took the sample out again. The contact angle behavior was the same as with a full XPS measurement, the CA increased significantly. Hence we concluded that the reason for the CA change during the measurements is due to some contamination within the vacuum system. The CA change was not only observed in the Kratos system but also in the Φ system. Since both systems are pumped by turbo pumps with mechanical fore pumps that contain oil, the conclusion suggests itself that hydrocarbons originating from the pumps could be the contamination. In order to check which kind of contamination is adsorbed on the sample surfaces in the vacuum systems, I introduced a sample into the Kratos system and measured it before and after with FTIR. The difference spectrum showed that hydrocarbons were added in the vacuum system. This is consistent with the relatively high carbon content detected with XPS. For a sample angle of 90° in the Kratos system the average measured carbon concentration on the samples is (26.8 ± 2.7) at%, for a sample angle of 45° it is (19.4 ± 1.9) at%. In the Φ system with the fixed sample angle of 45° , the average measured carbon concentration on the samples is (14.0 ± 1.4) at%.

To estimate the thickness of the hydrocarbon layer, equation (4.4) can be solved for the thickness d :

$$d = -\lambda \cdot \ln \left(1 - \frac{I}{I_0} \right) \cdot \sin(\alpha) \quad (5.2)$$

where λ is the electron attenuation length in the overlayer for the according kinetic energy of the photoelectrons, $\frac{I}{I_0}$ is the measured atomic concentration of the overlayer and α is the real take off angle of the measured photoelectrons. As attenuation length I used a reported value for hydrocarbons for the intermediate kinetic energy of O1s ($E_{kin,O1s} \approx 955\text{eV}$) $\Rightarrow \lambda \approx 28 \text{ \AA}$ [38, 39]. To get an upper limit of the overlayer thickness α is set to 90° . In that case, with the measured average carbon concentration of 19.4% in the Kratos system, $d = 6.0 \text{ \AA}$, the measured concentration in the Φ system of 14.0% results in an overlayer thickness of $d = 4.2 \text{ \AA}$.

5.3 FTIR measurements

FTIR is a vibrational spectroscopy and can provide information about chemical bonds. Hence combined with a technique like XPS which can determine atomic species, it is a powerful method for investigating processes on surfaces.

5.3.1 Measurements

The measurements presented here were performed with a Thermo Nicolet 6700 FTIR spectrometer. One experiment consists of two measurements. First a reference single-beam spectrum is taken of the sample before the sample treatment. Then a sample treatment is applied, for example, a sample with high CA is UV irradiated or a sample with low CA is stored at 50°C in an oxygen atmosphere for 20 h to increase the CA. After the treatment, when the property of interest has changed, the second single-beam spectrum is taken. In order to obtain the information about what changed on the surface during the treatment or what changed the investigated property, respectively, the two single-beam spectra are processed by ratioing the single-beam spectrum after the treatment with the reference spectrum before the treatment. The obtained sample spectrum contains information about added, subtracted and changed chemical bonds due to the treatment.

With FTIR we did basically the same measurement cycle as with XPS. The first single-beam spectrum was acquired directly after the growth of the ZnO nanotips after a CA measurement. This is the first reference spectrum. Then the sample was heat-treated by annealing it to 50°C for 20 h in a chamber with oxygen flow to increase the CA. After the CA was increased, we measured the CA and the second FTIR single-beam spectrum. By UV irradiation we decreased the CA again, measured the CA and acquired the third single-beam spectrum. This was the first complete measurement cycle. Since always a reference spectrum is needed, two sample spectra are obtained out of the three measured single-beam spectra of one cycle. Peaks pointing upward in the spectra indicate added bonds during the treatment, downward pointing peaks indicate removed bonds.

5.3.2 Results

Figure 5.16 shows two sample spectra after annealing, both processed with a reference spectrum taken directly after growth. In this case the CA after the first annealing was

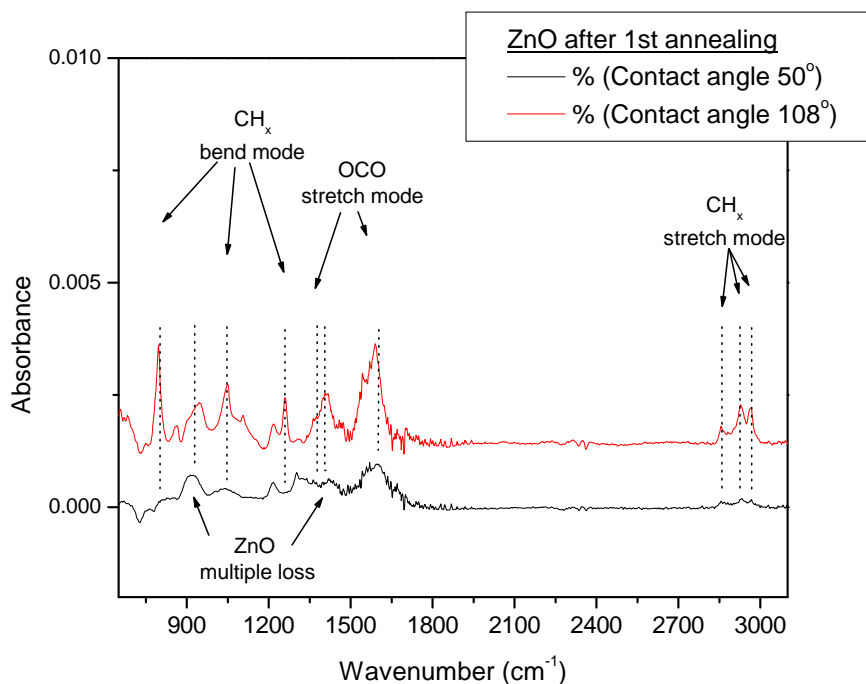


Figure 5.16: FTIR sample spectra after annealing the sample, both with the same reference spectrum taken directly after growth. The CH_x features increase with the CA from 50° to 108°.

only 50°, then the annealing was continued to obtain a CA of 108°. The peaks in the region from about 2850 cm⁻¹ to 2980 cm⁻¹ are CH_x stretching modes and arise from adsorbed hydrocarbons. There are three distinct peaks in this area at 2857 cm⁻¹, 2928 cm⁻¹ and 2965 cm⁻¹. Also arising from hydrocarbons are the CH_x bending modes, visible in these spectra at 800 cm⁻¹, 1050 cm⁻¹ and 1260 cm⁻¹. From these spectra it seems to be that with increasing CA hydrocarbons are added since the peak area under the CH_x related features increases significantly from 50° to 108°. There are also other features that can be ascribed to OCO stretching modes at 1380 cm⁻¹ and 1600 cm⁻¹ and ZnO multiple loss features at 930 cm⁻¹ and 1400 cm⁻¹ which arise from ZnO phonon modes. The COC stretching modes and the ZnO phonon modes were observed

on most of the measured spectra but they are not consistent with the according CA data in terms of not always pointing in the expected direction or not changing the peak area in the right amount.

One complete cycle and a second annealing after it is shown in Figure 5.17. Here

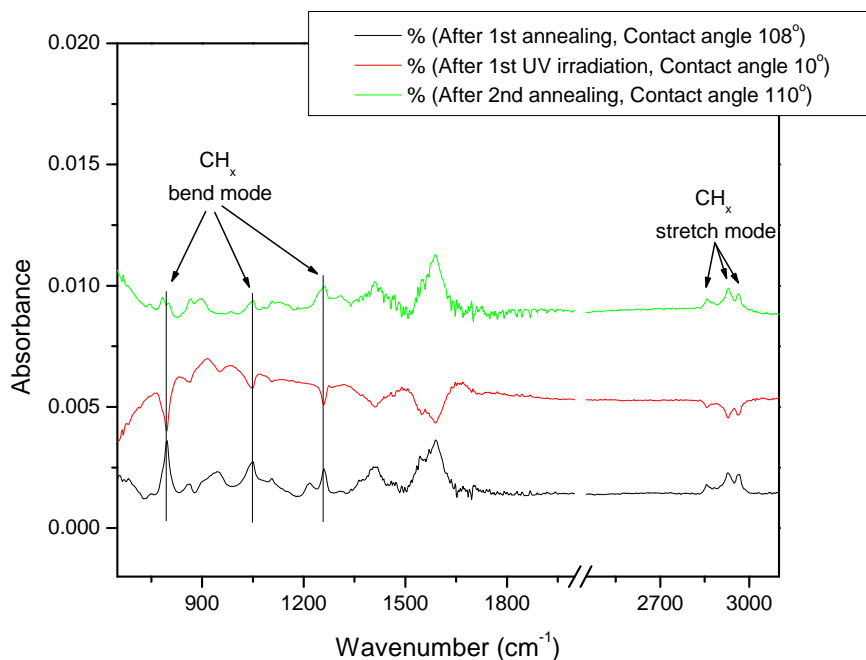


Figure 5.17: FTIR Sample spectra after the first annealing, after the first UV irradiation and after the second annealing. The references were in each case the single-beam spectra of the step before.

each spectrum was processed with the single-beam spectrum from the previous step as reference. The spectrum with the CA of 108° is the same as in Figure 5.16. The second one was taken after UV irradiation; the measured CA after the UV treatment was 10°. The reference was the spectrum of the step before with a CA of 108°. The peaks pointing down indicate the removal of the indicated CH_x species. After the second annealing the sample showed a CA of 110°, and the spectrum taken with the single-beam spectrum of the previous step as reference shows again the addition of hydrocarbons. If the peak areas are compared, the area removed by UV irradiation is identical to the peak area after the first annealing which indicates that mainly all the hydrocarbons are removed. After the second annealing, it appears that the same area is added again. If the error

bars are taken into account it means that roughly the same coverage of hydrocarbons adsorbs and desorbs.

5.4 Conclusion

This thesis describes the investigation of controlled CA changes induced by UV irradiation and dark storage on nanostructured ZnO surfaces grown by metalorganic chemical vapor deposition (MOCVD). The investigated surfaces consist of dense arrays of slender ZnO nanotips with a high aspect ratio. The typical tip height we used was about 500 nm, the average width about 80 nm. Directly after the growth the ZnO nanotip surfaces are hydrophilic with a CA of about 10° to 20° . If stored in the dark, the surfaces become hydrophobic with a CA maximum value of 100° to 110° . This usually takes at least one month if no special treatment is applied. We were able to shorten this time to about 20 hours by annealing the samples to 50° for about 20 hours in a chamber with oxygen flow. UV irradiation of a hydrophobic ZnO surface decreases the CA to values less than 5° within 5 to 30 min, depending on the intensity of the UV lamp. The measured intensity of the two UV lamps used are 2 mW/cm^2 and 3.6 mW/cm^2 . The surface roughness has a big influence on the reached CA values. On flat films the observed minimum and maximum CA values were 45° and 90° , respectively.

In order to gain insight into the mechanisms of the controlled wettability at the atomic level we used surface-sensitive spectroscopic methods: x-ray photoelectron spectroscopy (XPS) and Fourier transform infrared spectroscopy (FTIR). XPS measurements showed no correlation between concentration of oxygen-containing species and CA changes. Carbon contamination in the vacuum systems, however changed the CA during the measurements to high values on the order of 100° . The estimated hydrocarbon layer thickness is lower than 6 \AA which is roughly about 1 ML to 1.5 ML. FTIR studies indicate that adding and removing of hydrocarbons probably plays a role in the CA change since they are almost completely removed by UV irradiation and added again after recovery from low to high CAs. Hence even a hydrocarbon layer of about 1 ML thickness seems to affect the macroscopic property of surface wettability.

Some of the results are preliminary and much more effort has to be made in order to get a real understanding of this complex topic. These ZnO surfaces seem to be very sensitive to carbon contamination in vacuum systems; in the future, the systems used have to be cleaned thoroughly and be operated by dry, clean, oil-free pumps. Further FTIR studies could be done in-situ, for example, in a chamber where the recovery process during heating can be studied in a controlled environment. Since neither XPS system showed any consistent trends, possibly with variation of the photon energy to more surface sensitive energies, for example, at a synchrotron, more information could be revealed about the mechanisms on the atomic level.

References

- [1] W. Barthlott, Z. Cerman, M. Spaeth, A. Solga, and C. Neinhuis. URL: http://www.botanik.uni-bonn.de/system/lotus/de/lotus_effect_html.html, June 2005.
- [2] R.N. Wenzel. Resistance of solid surfaces to wetting by water. *Industrial and Engeneering Chemistry*, 28:988–994, 1936.
- [3] A.B.D. Cassie and S. Baxter. Wettability of porous surfaces. *Transaction of the Faraday Society*, 40:546–551, 1944.
- [4] J. Bico, C. Marzolin, and D. Quéré. Pearl drops. *Europhysics Letters*, 47 (2):220–226, 1999.
- [5] N.A. Pantakar. On the Modeling of Hydrophobic Contact Angles on Rough Surfaces. *Langmuir*, 19:1249–1253, 2003.
- [6] T. Onda, S. Shibuich, N. Satoh, and K. Tsujii. Super-Water-Repellent Fractal Surfaces. *Langmuir*, 12(9):2125–2127, 1996.
- [7] Lin Feng, Shuhong Li, Yingshun Li, Huanjun Li, Lianjuan Zhang, Jin Zhai, Yanlin Song, Biqian Liu, Lei Jiang, and Daoben Zhu. Super-Hydrophobic Surfaces: From Natural to Artificial. *Advanced Materials*, 14:1857–1860, 2002.
- [8] D. Öner and T.J. McCarthy. Ultrahydrophobic Surfaces. Effects of Topography Length Scales on Wettability. *Langmuir*, 16(20):7777–7782, 2000.
- [9] A. Zangwill. *Physics at Surfaces*. Cambridge University Press, 1988.
- [10] University Leiden, Leiden (NL). *Mimicking nature: Physical basis and artificial synthesis of the Lotus-effect.*, 2003.
- [11] M. Farnsworth and C.H. Kline. *Zinc Chemicals*. International lead zinc research organization, Inc., 2nd edition, 1983.
- [12] B.J. Coppa, R.F. Davis, and R.J. Nemanich. Gold Schottky contacts on oxygen plasma-treated, *n*-type ZnO (000 $\bar{1}$). *Applied Physics Letters*, 82(3):20, January 2003.
- [13] C.R. Gorla, N.W. Emanetoglu, S. Liang, W.E. Mayo, Y. Lu, M. Wraback, and H. Shen. Structural, optical, and surface acoustic wave properties of epitaxial ZnO films grown on (01 $\bar{1}$ 2) sapphire by metalorganic chemical vapor deposition. *Journal of Applied Physics*, 85(5):2592–2602, March 1999.
- [14] S. Muthukumar, H. Sheng, Z. Zhong, Z. Zhang, N.W. Emanetoglu, and Y. Lu. Selective MOCVD Growth of ZnO Nanotips. *IEEE Transactions on Nanaotechnology*, 2:50–54, 2003.

- [15] URL: <http://cst-www.nrl.navy.mil/lattice/struk/b4.html>, June 2005.
- [16] V.E. Henrich and P.A. Cox. *The surface science of metal oxides*. Cambridge University Press, 1994.
- [17] U. Diebold, L. Koplitzb, and O. Dulub. Atomic-scale properties of low-index ZnO surfaces. *Applied Surface Science*, 237:336–342, 2004.
- [18] Olga Dulub, Ulrike Diebold, and G. Kresse. Novel Stabilization Mechanism on Polar Surfaces: ZnO(0001)-Zn. *Physical Review Letters*, 90(1):016102, 2003.
- [19] A. Wander, F. Schedin, P. Steadman, A. Norris, R. McGrath, T.S. Turner, G. Thornton, and N. M. Harrison. Stability of Polar Oxide Surfaces. *Physical Review Letters*, 86(17):3811–3814, 2001.
- [20] D.C. Look, J.W. Hemsky, and J.R. Sizelove. Residual native shallow donor in ZnO. *Physical Review Letters*, 82:2552–2555, March 1999.
- [21] van der Walle C.G. Hydrogen as a cause of doping in zinc oxide. *Physical Review Letters*, 85:1012–1015, 2000.
- [22] B. Meyer and C. Wöll. Partial Dissociation of Water Leads to Stable Superstructures on the Surface of Zinc Oxide. *Angewandte Chemie International Edition*, 43:6642–6645, 2004.
- [23] J. Zhong, S. Muthukumar, Y. Chen, Y. Lu, H.M. Ng, W. Jiang, and E.L. Garfunkel. Ga-doped ZnO single-crystal nanotips grown on fused silica by metalorganic chemical vapor deposition. *Applied Physics Letters*, 83:3401–3403, 2003.
- [24] D.P. Woodruff and T.A. Delchar. *Modern Techniques of Surface Science - Second Edition*. Cambridge Solid State Science Series. Cambridge University Press, 1994.
- [25] D. Briggs and M.P. Seah, editors. *Practical Surface Analysis SECOND EDITION Volume 1 Auger and X-ray Photoelectron Spectroscopy*. John Wiley & Sons Ltd. Baffins Lane, Chichester, West Sussex PO19 1UD, England, Otto Salle Verlag GmbH & Co., Frankfurt am Main, Verlag Sauerländer AG, Aarau, 1990.
- [26] S. Wartewig. *IR and Raman Spectroscopy Fundamental Processing*. WILEY-VCH GmbH & Co. KGaA, 2003.
- [27] Brian C. Smith. *Fundamentals of Fourier Transform Infrared Spectroscopy*. CRC Press, Inc., 1996.
- [28] Yves J. Chabal. Script to lecture: Surface Science II, Rutgers, the State University of New Jersey. 2005.
- [29] Robert J. Bell. *Introductory Fourier Transform Spectroscopy*. Academic Press, Inc., Orlando, Florida 32887, 1972.
- [30] Finn Knut Hansen. DROPimage; a program system for interfacial tension and contact angle measurements by image analysis; Advanced Edition. Copyright © 1990-2005 Finn Knut Hansen. Printed in the USA.

- [31] Jing Liqiang, Xin Baifu, Yuan Fulong, Wang Baiqib, Shi Keying, Cai Weimin, and Fu Honggang. Deactivation and regeneration of ZnO and TiO₂ nanoparticles in the gas phase photocatalytic oxidation of *n*-C₇H₁₆ or SO₂. *Applied Catalysis A: General*, 275:49–54, 2004.
- [32] Liqiang Jing, Zili Xu, Xiaojun Sun, Jing Shang, and Weimin Cai. The surface properties and photocatalytic activities of ZnO ultrafine particles. *Applied Surface Science*, 180:308–314, 2001.
- [33] http://www.lot-oriel.com/site/pages_de_en/products/light_sources/light_sources.php, July 2005.
- [34] Ren-De Sun, Akira Nakajima, Akira Fujishima, Toshiya Watanabe, and Kazuhito Hashimoto. Photoinduced Surface Wettability Conversion of ZnO and TiO₂ Thin Films. *Journal of Physical Chemistry B*, 105:1984–1990, 2001.
- [35] Xinjian Feng, Lin Feng, Meihua Jin, Jin Zhai, Lei Jiang, and Daoben Zhu. Reversible Super-hydrophobicity to Super-hydrophilicity Transition of Aligned ZnO Nanorod Films. *Journal of the American Chemical Society*, 126:62–63, 2004.
- [36] K. Ogata, T. Komuro, K. Hama, K. Koike, S. Sasa, M. Inoue, and M. Yano. Characterization of undoped ZnO layers grown by molecular beam epitaxy towards biosensing devices. *Physical Status Solidi B*, 241:616–619, 2004.
- [37] B.J.Coppa and R.F.Davis. Gold Schottky contacts on oxygen plasma-treated, *n*-type ZnO(000 $\bar{1}$). *Applied Physics Letters*, 82:400–402, 2003.
- [38] Colin D. Bain and George M. Whitesides. Attenuation Lengths of Photoelectrons in Hydrocarbon Films. *Journal of Physical Chemistry*, 93:1670–1673, 1989.
- [39] Paul E. Laibinis, Colin D. Bain, and George M. Whitesides. Attenuation of Photoelectrons in Monolayers of *n*-Alkanethiols Adsorbed on Copper, Silver, and Gold. *Journal of Physical Chemistry*, 95:7017–7021, 1991.

Vita

Andreas Johannes Nuber

- 15. June 1980** born in Weingarten (Germany)
- 1987-1991** Grundschule Buchenberg
- 1991-2000** Allgäu-Gymnasium Kempten
- Summer 2000** Abitur
- 2001-2003** Undergraduate student of Physics at Julius-Maximilians-Universität Würzburg, Germany
- Summer 2003** Diplomvorprüfung
- 2003-2004** Graduate student of Physics at Julius-Maximilians-Universität Würzburg, Germany
- 2004-2005** Graduate student, Rutgers University
- October 2005** M.S. in Physics from Rutgers University (advisor: Professor T.E. Madey)